


Active site architecture reveals coordination sphere flexibility and specificity determinants in a group of closely related molybdoenzymes

Received for publication, December 24, 2020, and in revised form, April 11, 2021. Published, Papers in Press, April 20, 2021.

<https://doi.org/10.1016/j.jbc.2021.100672>

Michel A. Struwe^{1,2}, Palraj Kalimuthu³, Zhenyao Luo^{1,4}, Qifeng Zhong¹, Daniel Ellis¹, Jing Yang⁵, K. C. Khadanand⁵, Jeffrey R. Harmer⁶, Martin L. Kirk⁴, Alastair G. McEwan¹, Bernd Clement², Paul V. Bernhardt³, Bostjan Kobe^{1,4}, and Ulrike Kappler^{1,*} 

From the ¹Australian Infectious Disease Research Centre, School of Chemistry and Molecular Biosciences, The University of Queensland, Brisbane, Qld, Australia; ²Pharmazeutisches Institut, Christian-Albrechts-Universität Kiel, Kiel, Germany; ³School of Chemistry and Molecular Biosciences, ⁴Institute for Molecular Bioscience, The University of Queensland, Brisbane, Qld, Australia; ⁵Department of Chemistry and Chemical Biology, The University of New Mexico, Albuquerque, New Mexico, USA; ⁶Centre for Advanced Imaging, The University of Queensland, Brisbane, Qld, Australia

Edited by F. Peter Guengerich

MtsZ is a molybdenum-containing methionine sulfoxide reductase that supports virulence in the human respiratory pathogen *Haemophilus influenzae* (Hi). HiMtsZ belongs to a group of structurally and spectroscopically uncharacterized S-/N-oxide reductases, all of which are found in bacterial pathogens. Here, we have solved the crystal structure of HiMtsZ, which reveals that the HiMtsZ substrate-binding site encompasses a previously unrecognized part that accommodates the methionine sulfoxide side chain *via* interaction with His182 and Arg166. Charge and amino acid composition of this side chain-binding region vary and, as indicated by electrochemical, kinetic, and docking studies, could explain the diverse substrate specificity seen in closely related enzymes of this type. The HiMtsZ Mo active site has an underlying structural flexibility, where dissociation of the central Ser187 ligand affected catalysis at low pH. Unexpectedly, the two main HiMtsZ electron paramagnetic resonance (EPR) species resembled not only a related dimethyl sulfoxide reductase but also a structurally unrelated nitrate reductase that possesses an Asp–Mo ligand. This suggests that contrary to current views, the geometry of the Mo center and its primary ligands, rather than the specific amino acid environment, is the main determinant of the EPR properties of mononuclear Mo enzymes. The flexibility in the electronic structure of the Mo centers is also apparent in two of three HiMtsZ EPR-active Mo(V) species being catalytically incompetent off-pathway forms that could not be fully oxidized.

Sulfoxides occur naturally in the environment and some can serve as alternative electron acceptors in bacterial anaerobic respiration (1). In aqueous environments, degradation of the algal osmoprotectant dimethyl sulfoniopropionate can lead to

the formation of dimethyl sulfoxide (DMSO), whereas other biologically relevant sulfoxides, such as methionine sulfoxide (MetSO) or biotin sulfoxide (BSO), form predominantly during cellular processes where reactive oxygen species are generated. These processes include aerobic respiration, and in mammals, the inflammatory response to pathogens and cell injury (1–3).

We have recently characterized a molybdenum-containing MetSO reductase, *Haemophilus influenzae* MtsZ (HiMtsZ), that is required for interactions of the human pathobiont *H. influenzae* with its host (4). *H. influenzae* typically persists asymptotically in the human nasopharynx but can cause acute respiratory tract diseases such as otitis media and pneumonia and is known to worsen chronic respiratory conditions such as chronic obstructive pulmonary disease, asthma, and bronchiectasis (5–8). In addition, *H. influenzae* has recently been identified as a major pathogen in respiratory tract coinfections in patients with COVID-19 (9). HiMtsZ is required for intracellular survival of *H. influenzae* in bronchial epithelial cells and *H. influenzae* fitness in a mouse model of lung infection, indicating an essential physiological role for the enzyme during infection (4).

HiMtsZ belongs to the DMSO reductase family of molybdoenzymes and is related to two well-characterized enzymes that mediate bacterial anaerobic respiration, the DorA DMSO reductase (DorA) from *Rhodobacter* sp., and the TorA trimethylamine N-oxide (TMAO) reductase (TorA) that has been characterized in *Escherichia coli* (Ec) and *Shewanella massilia* (Sm) (10–14). In all of these enzymes, the active site contains a molybdenum atom that is coordinated by the dithiolene sulfurs of two organic pyranopterin guanine dinucleotide (PGD) cofactors (15–17). Additional ligands of the Mo atom are an amino acid ligand, which for Dor/Tor enzymes is a serine, and a water-based ligand (15, 18). This water-based ligand is involved in catalysis, and the electrons required for the reduction of the substrate molecules are supplied *via* the cellular quinone pool and a membrane-bound cytochrome

* For correspondence: Ulrike Kappler, u.kappler@uq.edu.au.

Present address for Michel A. Struwe: Zoologisches Institut - Strukturbiologie, Christian-Albrechts-Universität zu Kiel, Kiel 24118, Germany.

Molecular basis of molybdenum enzyme diversification

(e.g., DorC/TorC/MtsY) (1, 17). Both DorA and TorA have undergone extensive characterization by a variety of methods including X-ray crystallography that revealed a conserved domain and fold-structure, as well as electron paramagnetic resonance (EPR), magnetic CD, and X-ray absorption spectroscopy (10, 19–25), whereas for other types of enzymes in this group, such as the BSO reductases (BisC), only limited kinetic and spectroscopic data are available (26, 27). No spectroscopic or structural data are currently available for MtsZ, and a limited characterization of its enzymatic properties revealed activity with both DMSO and racemic MetSO (*rac*MetSO), as well as, to a lesser extent, BSO (4).

We have previously published a detailed phylogenetic analysis of Dor-/Tor-type enzymes, which shows that DorA and TorA form a distinct phylogenetic group (group 1) (Fig. S1), while HiMtsZ is part of a second group (group 2) that also includes the BisC and a putative TMAO reductase from *Ec*, TorZ (4), both of which have only undergone partial characterization. A third group is formed by enzymes related to a biotin sulfoxide reductase from *Rhodobacter sphaeroides* (Rs) (Fig. S1).

Interestingly, all three enzymes in the second group are able to reduce MetSO (4, 28, 29) and, like MtsZ, BisC also appears to have a role in host–pathogen interactions (30). The potential shift in the physiological roles of the group 2 enzymes is also reflected in changes in the types of, and affinities for, different S- and N-oxides these enzymes convert. Although both DorA and TorA have low micromolar K_M values (0.007 and 0.07 mM, respectively) for their preferred substrates, DMSO and TMAO (11, 12, 31, 32), in the group 2 enzymes, the lowest K_M values are observed for RS_C - S_S -MetSO (0.017 mM) in BisC, and, to a lesser extent, BSO (0.36 mM) in the *Ec* TorZ enzyme (28, 33) (Table 1). These differences in kinetic properties and substrate specificity between the group 1 and group 2 Dor-/Tor-type enzymes may be associated with

a niche-specific evolution of biological function to facilitate, for example, the interaction of a bacterial pathogen with the host. The high degree of structural and sequence similarity between Dor-/Tor-type enzymes then raises the intriguing question of how the underlying chemistry is tuned to enable functional differences to emerge.

Here, we have used a combination of structural, kinetic, electrochemical, and spectroscopic investigations of recombinant HiMtsZ to better understand the molecular and evolutionary relationships between the enzymes of the Dor/Tor groups.

Our investigations provide new insights into the evolution of substrate binding and the role of the direct ligand environment of the Mo atom in determining the EPR spectroscopic properties of the DMSO reductase family of molybdoenzymes. This work challenges the long-accepted concept of Mo-enzyme spectroscopic signatures being linked to particular types of enzymes.

Results

The HiMtsZ crystal structure reveals significant similarity to the structures of other respiratory Dor/Tor enzymes

The crystal structure of recombinant HiMtsZ at pH 7.0 ($R_{\text{free}} -15.4\%$, resolution 1.73 Å) consists of 765 amino acid residues (residues 43–420, 434–766, and 772–825), 722 water molecules, two Mo–PGD ligands, one molybdenum atom with a water-based ligand, one chloride ion, and three Hepes molecules (Table 2). Two loop regions (residues 421–433 and 767–771) are disordered and are not included in the model. The HiMtsZ 421 to 433 region is equivalent to a loop that is also disordered in the structure of *Rhodobacter capsulatus* (Rc) DorA (PDB ID: 1DMS) (21). The HiMtsZ structure shows the typical four-domain architecture also found in DorA (PDB ID: 1EU1; 1DMS) (21) and TorA (PDB ID: 1TMO) (10), where domains I–III form a funnel-like structure that is capped by the C-terminal domain IV (Fig. 1, Figs. S2–S4, Table S1).

The four structural domains are noncontiguous in the protein sequence except for the C-terminal domain IV. All domains contain a mix of β -sheets and α -helices, as described in detail (20), and domain I is the only domain that forms no interactions with the Mo cofactor (20). Domains II and III have an α - β architecture and share some general fold similarity (Fig. S3), which has been suggested to have arisen as both domains bind the guanine moieties of the cofactor (20).

A Dali search indicates that the HiMtsZ structure is most similar to the *Rhodobacter* sp. DorA structures (RMSD = 1.3 Å, z-score: 53.2 (Rc) and 52.0 (Rs), respectively) (Fig. S5). This was expected because no crystal structures for any other group 2 Dor/Tor enzymes such as EcBisC or EcTorZ are currently available (4) (Figs. S1 and S5).

The HiMtsZ active site and substrate access channel

As anticipated based on the overall structural similarity of HiMtsZ and Rc/RsDorA, the HiMtsZ active site is located at the bottom of the substrate access funnel formed by domains I to III; however, the residues surrounding the active site belong

Table 1
Catalytic parameters of Dor- and Tor-type enzymes

Substrate	Catalytic parameters	DMSO	MetSO	BSO	TMAO
<i>Rc</i> DorA (12)	K_M [μM]	9.7	-	-	193
	k_{cat} [s^{-1}]	43	-	-	134
<i>Rs</i> DorA (31)	K_M [μM]	7	330	-	2300
	k_{cat} [s^{-1}]	50	58	-	68
<i>Ec</i> TorA (11)	K_M [μM]	n.d.	n.d.	-	70
	k_{cat} [s^{-1}]	<4	<4	-	150
<i>Sm</i> TorA (88)	K_M [μM]	n.d.	n.d.	-	17
	k_{cat} [s^{-1}]	<4	<4	-	118.9
HiMtsZ (4)	K_M [μM]	140	410	1520	6700
	k_{cat} [s^{-1}]	85.4	91.7	182.6	434
<i>Ec</i> BisC (28)	K_M [μM]	-	17 ^a	-	-
	k_{cat} [s^{-1}]	-	-	-	-
<i>Ec</i> TorZ (29)	K_M [μM]	n.d.	800	360	1440
	k_{cat} [s^{-1}]	-	-	-	-
<i>Rs</i> BisC (26)	V_{max}^b	9	28	11.6	166
	K_M [μM]	14,440	850	15	11,050
	k_{cat} [s^{-1}]	-	-	-	-
	V_{max}^c	0.9	0.9	0.9	0.9

2-PicNO, 2-picoline N-oxide; LDAO, N,N-dimethyldodecylamine N-oxide (also: DDAO); n.d., not determined.

Units: K_M , μM ; k_{cat} , s^{-1} .

^a RS_C - S_S -MetSO.

^b V_{max} reported as [M s^{-1}].

^c V_{max} reported as [$\mu\text{mol min}^{-1} \text{nmol}^{-1}$].

Table 2
X-ray data collection and structure refinement parameters for HiMtsZ crystal structures

Catalytic parameters	pH 7.0	pH 5.5
Crystallization conditions	100 mM Na-Hepes 22% PEG 3350	100 mM Na-citrate 100 mM MetSO 22% PEG 3350
Diffraction source	MX1, Australian Synchrotron	
Temperature	100 K	100 K
Resolution	46.84–1.73 Å (1.73–1.77) ^a	46.86–2.09 Å (2.09–2.15) ^a
Unique reflections	75,666 (3691)	48,647 (38,818)
Space group	P 21 21 21	P 21 21 21
Cell (a, b, c)	58.2 Å, 93.68 Å, 132.78 Å	60.47 Å, 100.16 Å, 132.86 Å
Cell (α, β, γ)	90°, 90°, 90°	90°, 90°, 90°
Completeness	99.3% (87.9%)	99.3% (91%)
R _{merge} (all I+ and I-) ^b , (89)	0.108 (0.638)	0.137 (0.629)
R _{pim} (all I+ and I-) ^b , (89)	0.031 (0.188)	0.039 (0.187)
R _{meas} (all I+ and I-) ^b , (90)	0.113 (0.685)	0.143 (0.657)
CC _{1/2} (all I+ and I-) ^b , (91)	0.999 (0.904)	0.997 (0.853)
Mean I/σ (I)	17.4 (4.0)	13.0 (4.1)
Multiplicity	13.3 (12.3)	13.3 (11.5)
R _{work} ^b	0.132	0.155
R _{free} ^b	0.160	0.190
Number of nonhydrogen atoms	5985	6006
RMSD (bonds)	0.010 Å	0.003 Å
RMSD (angles)	1.18°	1.01°
Average B-factor	21.2 Å ²	35.0 Å ²
Ramachandran outliers	0 (0%)	0 (0%)
Side chain rotamer outliers	7 (1.1%)	6 (0.9%)
Clashscore	2	2

^a Values in parentheses correspond to the highest-resolution shell.^b Reported by XDS.

mostly to domains II and III. The Mo atom is coordinated by four dithiolene sulfur donor atoms originating from the bis-Mo-PGD cofactor (S-Mo distances: 2.27–2.41 Å), the O^γ of

Ser187 (1.95 Å), and a terminal water-based ligand at a distance of 2.34 Å, resulting in a distorted trigonal prismatic geometry (Fig. 1A, Table S2). The bond length of 2.34 Å

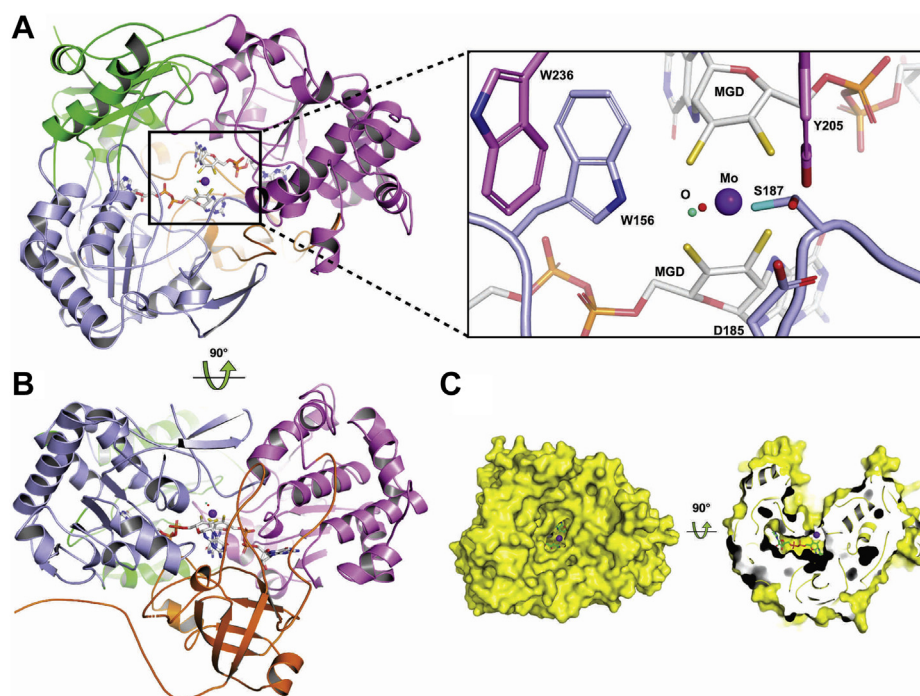


Figure 1. HiMtsZ domain and active site structure at pH 7.0. A, general fold of HiMtsZ and the structure of the HiMtsZ active site. The four structural domains are shown in different colors. N-terminal domain I (green), domain II (pink), domain III (light blue), C-terminal domain IV (orange). The 'call out' shows the HiMtsZ active site with key residues labeled. The two alternative configurations of Ser187 are shown with the oxygen molecules of the serine and the corresponding Mo aquo-ligand labeled in turquoise (hexacoordinate structure with an approximately trigonal prismatic shape, 80% occupancy) and red (pentacoordinate structure, 20% occupancy). B, HiMtsZ structure rotated by 90°. The coloring of the domains is as set out for panel A. C, HiMtsZ substrate access area. HiMtsZ is shown in yellow. Left panel, the view of the Mo active site from the outside. Right panel, 90° rotated view, presenting a section through HiMtsZ, with the substrate access funnel located at the top of the protein. HiMtsZ, *Haemophilus influenzae* MtsZ.

Molecular basis of molybdenum enzyme diversification

suggests that the ligand is probably in a hydroxide or aqua form (*cf.* the shorter $\text{Mo}^{\text{VI}} = \text{O}$ (oxido): $\sim 1.7 \text{ \AA}$ bond length (34)) possibly as a result of photoreduction of the resting Mo^{VI} oxidation state during data collection. An interesting feature of this structure is the presence of some disorder at the active site where, in an alternate conformation, Ser187 (Domain II) is dissociated from the Mo ion leaving the metal in a five-coordinate configuration. The relative occupancies of the six-coordinate (Ser-bound) and five-coordinate (Ser-dissociated) forms was 80:20 (Fig. 1A).

Two conserved residues, Tyr154 and Trp156 (domain II), which have previously been shown to be essential for the reduction of S- and N-oxides (12, 31), are located in proximity to the Mo atom, and together with three other conserved residues (HiMtsZ: Tyr205, Trp236, and Tyr400, all domain III) form a narrow hydrophobic pocket near the active site, which is in agreement with the DorA and TorA active sites (10, 14, 35) (Fig. 1A). DorA crystal structures with DMSO bound show that this hydrophobic pocket promotes the correct orientation of the sulfoxide substrate relative to the Mo center (14).

The two HiMtsZ PGD cofactors that coordinate the Mo center, designated P- and Q-PGD, form hydrogen bonds with residues in domains II and III, and are comparatively symmetrical in structure, with differences in torsion angles between the planar pterin and the puckered pyran moiety of only 8.6° (α -angles, a-b-c-d) and 22.4° (β -angles, a-b-c-e), respectively (Fig. 1A, Table S3). This is similar to what was seen for Sm TorA (1TMO) with $\alpha = 13.2^\circ$ and $\beta = 15.6^\circ$ and RsDorA (PDB ID: 1EU1, $\alpha = 12.4^\circ$, $\beta = 16.7^\circ$) but differs from other *Rhodobacter* DorA structures (PDB IDs: 1DMS, 1DMR, 2DMR, 3DMR, 4DMR, 1E5V, 1H5N), where angles between 12.4 to 22.7° (α) and 16.7 to 38.2° (β) were found (Table S3). This is an interesting observation, as torsion angles of the pyranopterin and PGD moieties are considered to be characteristic for different types and families of Mo enzymes (36).

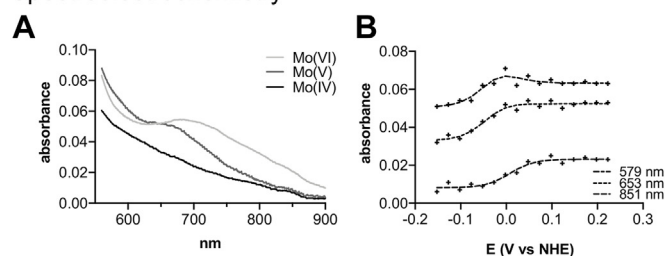
A narrow cavity connects the HiMtsZ Mo center to the substrate access funnel, which has an overall positive surface charge because of the presence of Arg166 and His182 (Fig. 1C, Figs. S3 and S4). The narrow opening near the Mo active site could prevent access of bulky substrates and might explain why HiMtsZ is incapable of reducing oxidized methionine residues found in proteins (4). For comparison, the Ec MsrP/YedY enzyme, a Mo-containing MetSO reductase from the sulfite oxidase enzyme family, has a much more openly accessible active site and is able to reduce protein-bound MetSO (37, 38).

Redox and EPR properties of the HiMtsZ active site reveal changes in redox and molecular properties compared with other Dor-/Tor-type enzymes

Using optical spectroelectrochemistry, we determined the $\text{Mo}^{\text{VI}/\text{V}}$ and $\text{Mo}^{\text{V}/\text{IV}}$ redox potentials of HiMtsZ, as electronic structure and associated redox potentials of the Mo center are known to affect the catalytic properties of Mo enzymes (36). This experiment is based on the change in absorbance of the Mo-PGD₂ chromophore as a function of the applied potential,

which is made possible by the absence of any other chromophores such as heme, Fe-S clusters, or flavin in HiMtsZ, which would mask redox-induced optical spectral changes at the Mo active site. In its resting, fully oxidized, Mo^{VI} state, the HiMtsZ electronic absorption spectrum exhibits a broad band maximum at 700 nm with less-pronounced shoulders observed at 520, 480, and 400 nm (Fig. 2A). These spectral features are similar to Rc and RsDorA DMSO reductases in a fully oxidized Mo^{VI} state (39, 40). As the potential was

Spectroelectrochemistry



EPR spectroscopy

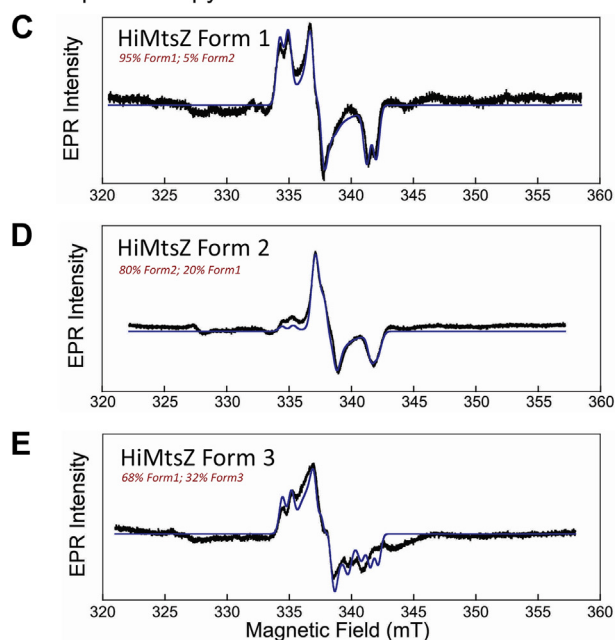


Figure 2. Redox and electron paramagnetic resonance properties of the HiMtsZ Mo center. Redox properties: A, calculated spectra of the Mo^{VI} , Mo^{V} , and Mo^{IV} forms of HiMtsZ from optical spectroelectrochemistry. B, single wavelength absorbance plots (579, 653, and 841 nm) versus electrochemical potential. The calculated redox potentials are $\text{Mo}^{\text{VI}/\text{V}} +11 (\pm 10)$ mV and $\text{Mo}^{\text{V}/\text{IV}} -49 (\pm 10)$ mV versus NHE (at pH 8). These potentials are in a similar region to those of *Rhodobacter sphaeroides* DMSO reductase (+83 and +37 mV versus NHE, pH 8.5) (42). Data were modeled with ReactLab Redox (Ver. 1.1, JPlus Consulting Pty Ltd) using a sequential two-electron transfer model. Electron paramagnetic resonance: C–E, 135K X-band EPR spectra of HiMtsZ forms 1 (C) 2 (D) and 3 (E) derived from redox titrations. The spin-Hamiltonian parameters determined from spectra simulations are listed in Table 1. EPR spectra for forms 1 and 2 were successfully simulated with a combination of both sets of spin-Hamiltonian parameters. HiMtsZ forms 1 and 2 display spectra that are very similar to low-pH and high-pH forms of EcNarGH, respectively. Form 1 was collected using an oxidation–reduction potential of +291 mV versus NHE, form 2 at +34 mV versus NHE, and form 3 at -7 mV versus NHE. Black lines—experimental data; blue lines—data from simulations. DMSO, dimethyl sulfoxide; Ec, *Escherichia coli*; EPR, electron paramagnetic resonance; HiMtsZ, *Haemophilus influenzae* MtsZ; NHE, normal hydrogen electrode.

lowered, the Mo^{VI} spectrum gave way to that of the intermediate Mo^V form with a maximum at 650 nm (Fig. 2A), which again is similar to a spectrum reported for RsDorA in its Mo^V form (41). Complete reduction to Mo^{IV} yielded a largely featureless absorption spectrum. Redox potentials of +11 (±10) mV for Mo^{VI/V} and -49 (±10) mV for Mo^{V/IV} versus normal hydrogen electrode (NHE) (at pH 8) were derived from the potential-dependent spectral data ($n = 2$ datasets) and demonstrate that the Mo^V oxidation state is only stable within a narrow potential window close to 0 V versus NHE (Fig. 2B). A similarly narrow Mo^V potential window, but with a more positive midpoint potential, was determined for RsDorA (Mo^{VI/V} and Mo^{V/IV} redox potentials +83 and +37 mV versus NHE, pH 8.5) (42).

Three EPR spectral forms (forms 1, 2, and 3) were observed for HiMtsZ during a redox titration with dithionite as the reductant and ferricyanide as the oxidant. None of these three forms displayed clearly discernible ^{95,97}Mo hyperfine coupling to the electron spin, but clear ¹H hyperfine coupling was observed for the form 1 spectrum (Fig. 2, C and D).

While being a minor component of these HiMtsZ EPR spectra, the form 3 EPR spectrum (Fig. 2E, Fig. S6) was able to be extracted *via* a global analysis of the potential dependent EPR redox titration data. The form 3 EPR spectrum is reminiscent of previously published Dor/Tor enzyme EPR spectra, including the high *g*-split DMSO reductase catalytic intermediate that was obtained under turnover conditions with TMAO as the oxidizing substrate (25, 41). Because the Mo^V signal of form 3 was only present within the same narrow Mo^V intermediate potential window defined by the optical spectroelectrochemistry experiments (Fig. 2B), we propose that form 3 likely represents the catalytically competent form of HiMtsZ in its paramagnetic Mo^V state.

Interestingly, the form 1 and form 3 EPR spectra possess similar *g*-tensors (Table 3). In addition, the form 1 HiMtsZ spectrum observed here not only resembles previously determined EPR spectra of Dor-/Tor-type enzymes but also possesses a remarkable similarity to the low pH (*lpH*) Mo^V form of the NarGH dissimilatory nitrate reductase (NarGH) Mo-containing nitrate reductase (43, 44). This implies that both form 1 HiMtsZ and *lpH* NarGH possess a similar 6-coordinate, distorted trigonal prismatic Mo^V active site geometry (Fig. 2E, Table S4) but with O_{Ser} coordinated to the metal in HiMtsZ form 1 instead of the O_{Asp} donor that is bound to Mo in *lpH* NarGH. Prominent ¹H hyperfine splitting

is observed on *g*₁ and *g*₃ in HiMtsZ form 1, with spectral simulations yielding an isotropic Fermi contact contribution to the ¹H hyperfine interaction ($A_{\text{iso}}^{\text{H}} = 20.3$ MHz) with a dipolar contribution of $A_{\text{S}}^{\text{H}} = [+4.7, -5.3, +0.7]$ MHz. The magnitude of the isotropic Fermi contact contribution to the measured hyperfine interaction is less than that observed for RsDorA ($A_{\text{iso}}^{\text{H}} = 31.3$ MHz; $A_{\text{S}}^{\text{H}} = [+6.8, -5.7, -1.2]$ MHz) or *lpH* NarGH ($A_{\text{iso}}^{\text{H}} = 27.4$ MHz $A_{\text{S}}^{\text{H}} = [+6.2, -2.7, -3.5]$ MHz), indicating less delocalization of the unpaired Mo electron spin onto this nucleus in HiMtsZ than in either DorA or NarGH. This likely results from small differences in the orientation of the, presumably, hydroxyl proton relative to the Mo redox orbital (45).

The potential-dependent EPR redox titration data (Fig. S7) reveal that while reduction of form 1 to its EPR-silent Mo^{IV} form is facile (E' (Mo^{V/IV}) -12 mV versus NHE), the species responsible for the form 1 Mo^V signal cannot be oxidized to its EPR-silent Mo^{VI} oxidation state. This unusual feature has been observed in potential-dependent EPR studies of other Mo enzymes (46, 47) and is now understood to derive from off-pathway, noncatalytically active forms of the protein where an exchangeable hydroxido/aqua ligand is absent (48) or access to this ligand is blocked. This is an important observation because a water-based ligand is essential to facilitate the electron transfer half-reactions that are coupled to deprotonation events (*i.e.*, Mo^{IV}-OH₂ → Mo^V-OH + e⁻ + H⁺ → Mo^{VI}≡O + e⁻ + H⁺). If this water-based ligand is absent or blocked, then the Mo active site is locked into its Mo^V form even at very high applied potentials (48). Although the nature of the exogenous ligand in form 1 that has replaced the hydroxido present in form 3 remains unknown, the nature of the ¹H hyperfine coupling indicates that a Mo^V-OH may indeed be present, but with a “blocked” or inaccessible proton acceptor.

Finally, the HiMtsZ form 2 spectrum was generated from a redox titration with 10% glycerol added to the buffer. Glycerol is a known inhibitor of DorA DMSO reductases (49), but glycerol concentrations up to 30% have no effect on HiMtsZ catalysis (Fig. 3). Upon addition of the dithionite reductant, an EPR spectrum emerged that resembles the spectra reported for the so-called ‘glycerol-inhibited’ form of DorA from Rc (49) and Rs (40) with similar *g*-values and no discernible ¹H hyperfine splitting (Fig. 2C). As was observed for the form 1 species, HiMtsZ form 2 also cannot be oxidized to the Mo^{VI} state although it can be reduced to the EPR-silent Mo^{IV} form

Table 3
EPR spin-Hamiltonian parameters for HiMtsZ and selected DMSO reductase family enzymes

Enzyme	<i>g</i> ₁	<i>g</i> ₂	<i>g</i> ₃	<i>g</i> _{ave}	A ₁ (H) ^b	A ₂ (H) ^b	A ₃ (H) ^b	A _{ave} (H) ^b
Nar <i>lpH</i> (43, 44)	2.001	1.985	1.964	1.983	33.6	24.7	23.9	27.4
Nar <i>hpH</i> (43, 44)	1.987	1.980	1.961	1.976	8.4	8.4	8.4	8.4
Rs DorA (25)	1.999	1.989	1.972	1.987	38.1	25.6	30.1	31.3
Rs DorA (glycerol inhibited) (40)	1.99	1.98	1.96	1.98	na	na	na	na
MtsZ form 1	2.001	1.985	1.959	1.982	25.0	15.0	21.0	20.3
MtsZ form 2	1.988	1.980	1.961	1.976	7.0	12.0	14.0	11.0
MtsZ form 3 ^a	1.991	1.9780	1.968	1.980	20	8	29	19

Nar, nitrate reductase; *hpH*, high pH; na, not available.
Hyperfine parameters are given in MHz.

^a The data used to generate these spin-Hamiltonian parameters had a low S/N ratio.

Molecular basis of molybdenum enzyme diversification

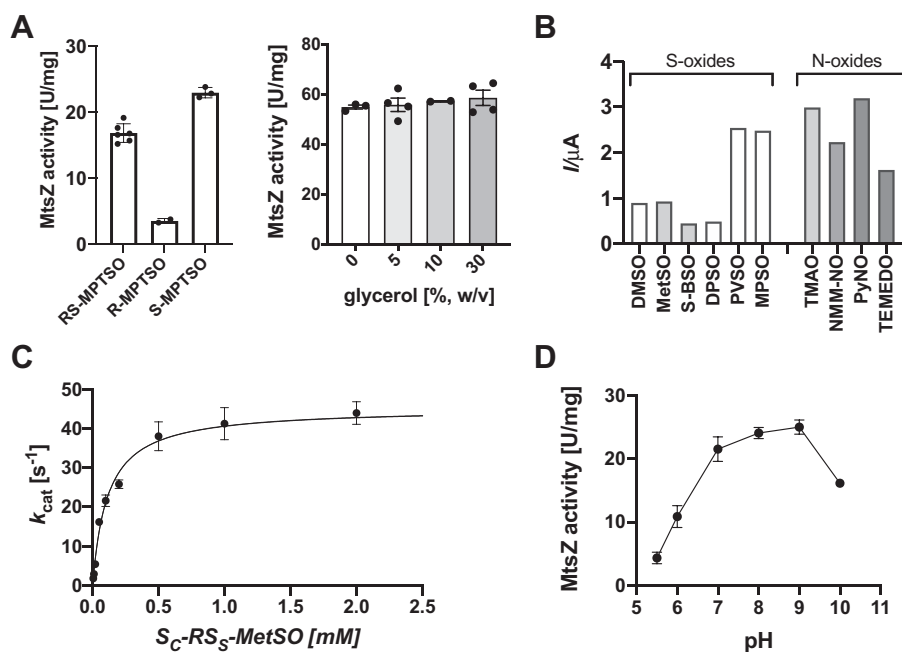


Figure 3. Characterization of HiMtsZ catalysis. *A, Left*, activity of HiMtsZ with different stereoisomers of MPTSO (methyl *p*-tolyl sulfoxide) showing a clear preference for the *S*- stereoisomer. *Right*, effect of glycerol on HiMtsZ activity with 10 mM DMSO at pH 8.0. Glycerol is a known inhibitor of DorA-type proteins but had no effect on HiMtsZ catalysis up to 30% glycerol. *B*, exploration of the HiMtsZ substrate range electrochemically driven catalysis at a GC/MtsZ electrode. *S*- and *N*-oxide substrates are shown. *C*, HiMtsZ activity with varying concentrations of *S*-*R*/*S*-MetSO (contains both sulfoxide stereoisomers) at pH 8.0 fit to the Michaelis–Menten equation. The data fit indicates a k_M L - R / S $MetSO_{app}$ of 0.115 ± 0.025 mM with a k_{cat} of 45.2 ± 2.6 s⁻¹. *D*, pH dependence of HiMtsZ activity with S_C -*R*/ S -MetSO, showing peak activity between pH 7 and 9. DMSO, dimethyl sulfoxide; DorA, DorA DMSO reductase; DPSO, dipropyl sulfoxide; GC, glassy carbon; MetSO, methionine sulfoxide; MPSO, methyl phenyl sulfoxide; NMM-NO, *N*-methyl morpholine *N*-oxide; PVSO, phenyl vinyl sulfoxide; Py NO, pyridine-*N*-oxide; S-BSO, *S*-biotin sulfoxide; TEMEDO, tetramethylethane-1,2-diamine dioxide; TMAO, trimethylamine *N*-oxide.

(E' (Mo^{V/IV}) ca. -50 mV versus NHE) (Fig. S7). The best spectral simulations of the experimental HiMtsZ EPR spectra from this experimental dataset were obtained by including ~20 to 30% of a form 1 component (Table 3), indicating a high degree of heterogeneity in the sample. The coordination geometry of form 2 is not known, but its inability to be oxidized to Mo^{VI} and lack of resolvable ¹H hyperfine indicate the absence of a water-based ligand in the first coordination sphere. Glycerol is an obvious candidate to occupy this position and block the active site from binding a water-based ligand, resulting in form 2 representing another off-pathway species. The fact that 30% glycerol does not affect HiMtsZ catalysis indicates that glycerol may bind to a catalytically incompetent form of the enzyme. Interestingly, the form 2 EPR spectrum also closely resembles the high pH spectrum that has previously been observed for NarGH.

HiMtsZ can reduce a wide variety of *S*- and *N*-oxides, with activity profiles affected by pH

To fully evaluate the substrate range and kinetic properties of HiMtsZ, we used viologen-based optical and electrochemically monitored assays. The voltammetric response of HiMtsZ on a glassy carbon (GC) electrode was characteristic of a catalytically homogeneous reaction, coupled to a heterogeneous electron transfer (EC' mechanism) (50). HiMtsZ catalysis on the GC electrode showed substrate concentration–dependent increases in the catalytic current for the previously identified substrates

*rac*MetSO, *S*-BSO, and TMAO, whereas no catalytic response was observed for the sulfur-based diastereomer *R*-BSO, which matches our previous results using optical enzyme assays (Fig. 4) (4). Saturation of the catalytic current at high substrate concentrations indicated that this is a true enzymatic reaction (Fig. 4). At low substrate concentrations, the appearance of a small prewave at ~ -360 mV (e.g., Fig. 4A, 800 μ M trace) indicated that the HiMtsZ reaction depleted the substrate in the vicinity of the electrode, causing the cyclic voltammetry (CV) electrode response to revert to that of the uncoupled, reversible $MV^{2+/+}$ response. This behavior has been described by us previously for different electrode surfaces and enzymes (51–53). Using BV^{2+} (-325 mV) as the redox mediator, similar responses were obtained, despite the smaller electrochemical driving force (Fig. S8).

We then used a combination of electrochemical and spectrophotometric assays to further investigate the substrate and stereospecificity of HiMtsZ catalysis. Using 10 mM *RS*-, *S*-, and *R*-methyl *p*-tolyl sulfoxide (MPTSO) as the substrate, we were able to confirm that HiMtsZ preferentially converts the sulfoxide *S*-enantiomer, as activity with *R*-MPTSO was only ~16% of the activity observed with *S*-MPTSO (Fig. 3A). As, unlike BSO that was used previously to assess enantioselectivity of HiMtsZ (4), both MPTSO enantiomers have equally accessible sulfoxide groups; this activity distribution directly reflects the chirality of the HiMtsZ active site. In activity tests with a variety of *S*- and *N*-oxides, catalysis was observed with methyl phenyl sulfoxide, phenyl vinyl sulfoxide, dipropyl sulfoxide, tetramethylethane-1,2-diamine dioxide, pyridine-*N*-oxide, and

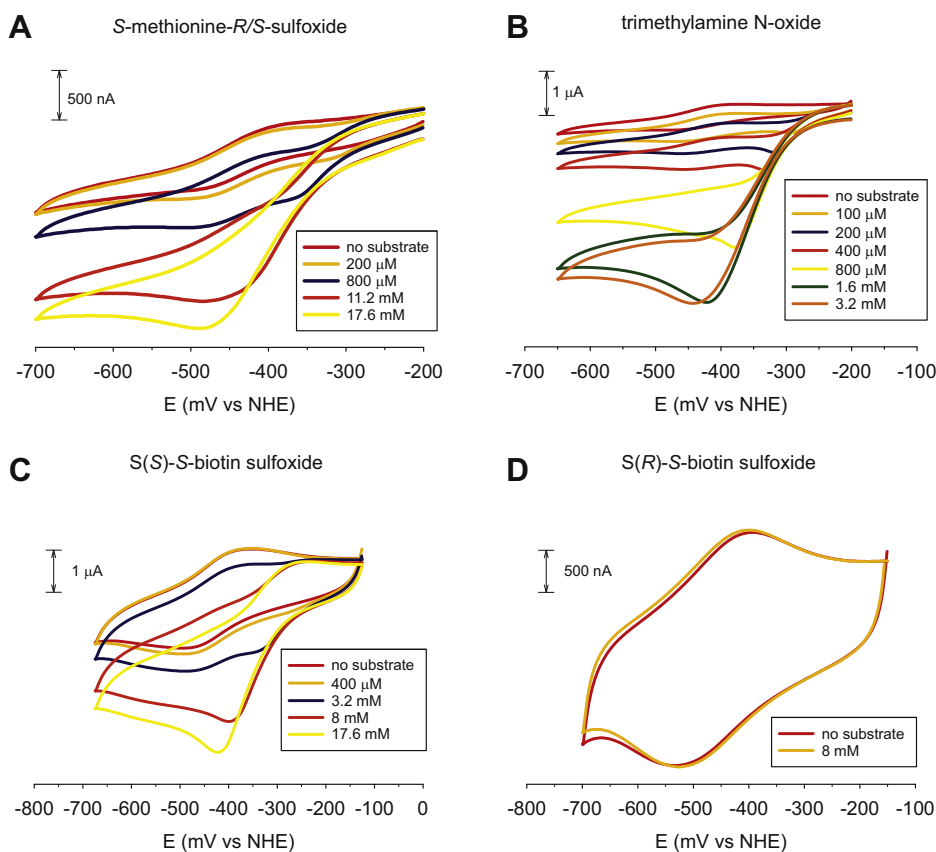


Figure 4. CVs obtained for the methyl viologen-mediated HiMtsZ reduction of substrates. A, *Sc*-methionine-*R/S*-sulfoxide with 50 μM MV^{2+} , B, trimethylamine N-oxide and 50 μM MV^{2+} , C, *S(S)*-*S*-biotin sulfoxide with 100 μM MV^{2+} , and D, *S(R)*-*S*-biotin sulfoxide with 100 μM MV^{2+} at a glassy carbon/HiMtsZ-modified electrode in 50 mM Tris Cl buffer (pH 8.0) at a scan rate of 5 mV s^{-1} . Substrate concentrations are shown in the figure legends. CV, cyclic voltammetry; HiMtsZ, *Haemophilus influenzae* MtsZ; MV, methyl viologen.

N-methyl morpholine N-oxide (Fig. 3B) but not the sterically demanding diphenyl sulfoxide, which significantly expands the range of known HiMtsZ substrates. We also achieved low levels of catalysis (~ 4 U/mg) with 6-hydroxyamino purine, a hydroxylamine that might occur in the human body, whereas nitrate and cysteine sulfinic acid were not reduced by HiMtsZ. A determination of kinetic parameters for *Sc-RS*-MetSO revealed a $k_{\text{cat,app}}$ of $45.5 \pm 2.5 \text{ s}^{-1}$ and a $K_{\text{M,app}}$ of $0.114 \pm 0.025 \text{ mM}$ (Fig. 3C). Based on the enantioselectivity of the HiMtsZ active site, *Sc-RS*-MetSO is unlikely to be converted and its presence in the reaction would thus likely cause some inhibitory effects through the formation of nonproductive enzyme-substrate complexes. This is also indicated by the 4-fold higher $K_{\text{M,app}}$ we determined earlier for *rac*MetSO ($K_{\text{M,app}} = 0.401 \text{ mM}$ (4)), where three of four MetSO forms present in the racemic mixture (Scheme S1) would not be able to be converted effectively by HiMtsZ. This suggests that the $K_{\text{M,app}}$ for *Sc-S*-MetSO, the likely natural substrate of this enzyme, may be up to a factor of 2 below the value determined for *Sc-RS*-MetSO.

At low pH, the serine ligand can dissociate from the HiMtsZ Mo center, causing inactivation of the enzyme

In our earlier work with HiMtsZ (4), a reaction lag was observed in some enzyme assays. This lag is similar to what has

been reported for other molybdoenzymes after recombinant expression, where redox-cycling of the enzyme with MV^+ in the presence or absence of substrate was able to resolve this issue (54). However, neither reduction of the amount of reductant in the assay nor incubation of HiMtsZ in the presence of reduced viologen dye before use in enzyme assays ('redox cycling') had any effect on the observed lag. Interestingly, when testing the pH dependence of HiMtsZ catalysis, where maximal activity was observed between pH 7.0 and 9.0 (Fig. 3D), it also became apparent that with increasing pH, the HiMtsZ reaction lag decreased. At pH 8.0 and above, no lag was observed (Fig. S9).

A second HiMtsZ crystal structure determined at pH 5.5 (resolution: 2 \AA , Fig. 5) reveals molecular changes that may explain the catalytic lag (Table 1). While the overall structure is essentially identical to the structure determined at pH 7.0 (RMSD = 0.5 \AA), Ser187 no longer coordinated the molybdenum (Mo-Ser187 O^{γ} distance: 4.09 \AA) at the active site. This dissociation is apparent although there is no change in the amino acid backbone position around the active site (0.07 \AA distance in $\text{C}\alpha$ positions) (Fig. 5, Fig. S10). In this low pH structure, the Ser187 side chain is within hydrogen-bonding distance of Asp185 and Tyr205, both of which are highly conserved in Dor-/Tor-type enzymes (Fig. S11). The pH 5.5 structure of the HiMtsZ active site is almost identical to that of the minor (20%) active site conformation observed in

Molecular basis of molybdenum enzyme diversification

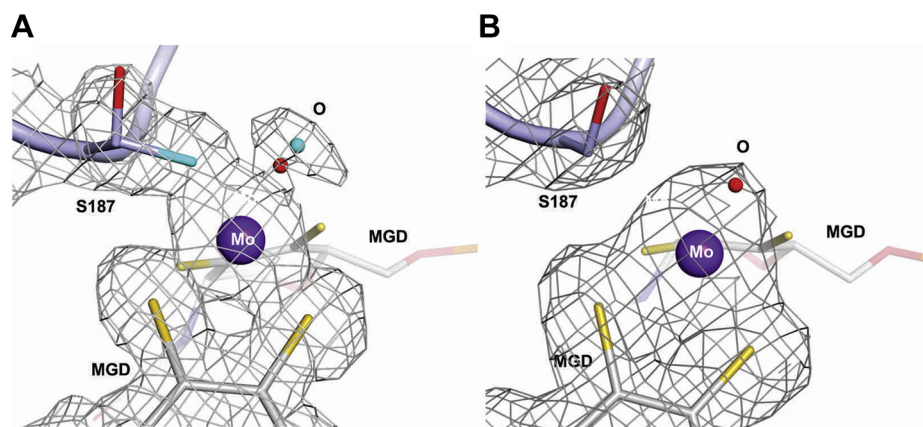


Figure 5. HiMtsZ active site structure and electron density observed at pH 7.0 and pH 5.5. The gray mesh represents a composite omit map (73) contoured at 1σ . The model is included in stick representation (white/light blue, carbon, main chain; yellow, sulfur; red, oxygen). *A*, active site at pH 7.0. Ser187 is coordinated to the molybdenum ion (occupancy of ligated conformation = 80%, shown in turquoise; occupancy of dissociated conformation = 20%, shown in red). The Mo-aquo ligand for each conformation is shown in the corresponding color. *B*, active site at pH 5.5. No electron density supporting Mo coordination by Ser187 is observed. HiMtsZ, *Haemophilus influenzae* MtsZ.

the pH 7 structure. As also indicated by the pH dependence of HiMtsZ activity (Fig. 3E), the dissociation of the Ser187 Mo ligand likely reduces HiMtsZ catalytic competency. This is similar to the effect of mutations of the serine ligand, which essentially abolish catalysis (6000-fold decrease) in a related BisC enzyme (55). Structural evidence for dissociation of the Mo amino acid ligand has not been previously reported in Dor-/Tor-type enzymes but has recently been proposed as an intermediate in an alternative mechanism of catalysis for a TorA TMAO reductase (56).

Substrate and stereospecificity of Dor-/Tor-type molybdenum enzymes correlate with subtle adjustments in surface properties near the active site

As the Dor-/Tor-type enzymes for which structures were solved previously convert small-molecule substrates such as DMSO or TMAO, residues involved in stabilizing interactions with sulfoxides that have significant side chains such as MetSO had not been identified. In this work, we were unable to obtain a HiMtsZ crystal structure with MetSO bound. As a result, to identify relevant residues in HiMtsZ, we used docking studies (Glide XP) with various sulfoxides. For the known HiMtsZ substrates, *S*-BSO, DMSO, and *S_C-S_S*-MetSO, Glide scores of -1.578 , -2.856 , and -3.316 kcal/mol, respectively, were obtained. These Glide scores indicate significant binding activities, and the respective magnitudes of the scores roughly correlate with the differences in HiMtsZ K_M values obtained for these substrates. For both docked DMSO and docked *S_C-S_S*-MetSO, the position of the sulfoxide group was similar and enabled interactions between the sulfur lone pair and Tyr154. In addition, the docked position of DMSO was nearly identical to the crystallographically determined orientation of DMSO bound to RcDorA (PDB: 4DMR). Similarly, *S*-MPTSO could be fit to the HiMtsZ active site in an orientation enabling interaction of Tyr154 with the *S*-oxide sulfur, but *R*-MPTSO could not fit in the active site. Neither *R*-BSO nor diphenyl sulfoxide could be fit to the HiMtsZ active site and neither could be reduced by HiMtsZ in kinetic assays.

In addition to the placement of the sulfoxide group near Tyr154, the interactions of *S_C-S_S*-MetSO with HiMtsZ also included a salt bridge between the *S_C-S_S*-MetSO carboxylic acid group and Arg166 and between His182 and the *S_C-S_S*-MetSO primary ammonium group (Figs. 6, B and C and 7). These stabilizing interactions could not be efficiently accessed by any of the other three MetSO stereoisomers, confirming our previous proposal that only *S_C-S_S*-MetSO is efficiently reduced by HiMtsZ.

Comparative analyses then revealed that HiMtsZ Arg166 and His182 are not conserved in either RcDorA, where they are replaced by Thr126 and Gly142, resulting in a neutral to slightly negative surface charge or SmTorA (Thr128, Lys144) (Fig. 6B). Only the equivalent of HiMtsZ His182 is present in the homology models of the other group 2 Dor/Tor enzymes, EcTorZ (His171), and EcBisC (His143) (supplemental Data S1 and S2) that are more closely related to HiMtsZ, while the arginine residue (HiMtsZ: Arg166) is replaced by either a glutamine (EcTorZ: Gln155) or a serine (EcBisC: Ser127), respectively (Fig. 6B). In these two enzymes, the positive charge of the substrate-binding region is further enhanced by the substitution of the nearby HiMtsZ Phe157 with an arginine (EcTorZ: Arg147, EcBisC: Arg118), which has the guanidinium group pointing toward the protein surface in the homology models.

The functional significance of these changes was revealed by further docking studies using RcDorA. Here, the presence of Gly142 and Thr126 prevents the formation of stabilizing interactions with the *S_C-S_S*-MetSO side chain, which is reflected in the absence of docking poses where the sulfoxide function was oriented toward the active site. However, this less-charged environment is highly suitable for the binding of DMSO, which does not possess any bulky functional groups, as indicated by a *Glide* docking score of -4.737 kcal/mol. For the first time, our docking studies have identified an additional component of the Dor-/Tor-type enzyme substrate-binding pocket that is located at a distance of ~ 10 to 12 Å from the Mo center. This pocket is highly variable in the different Dor-/

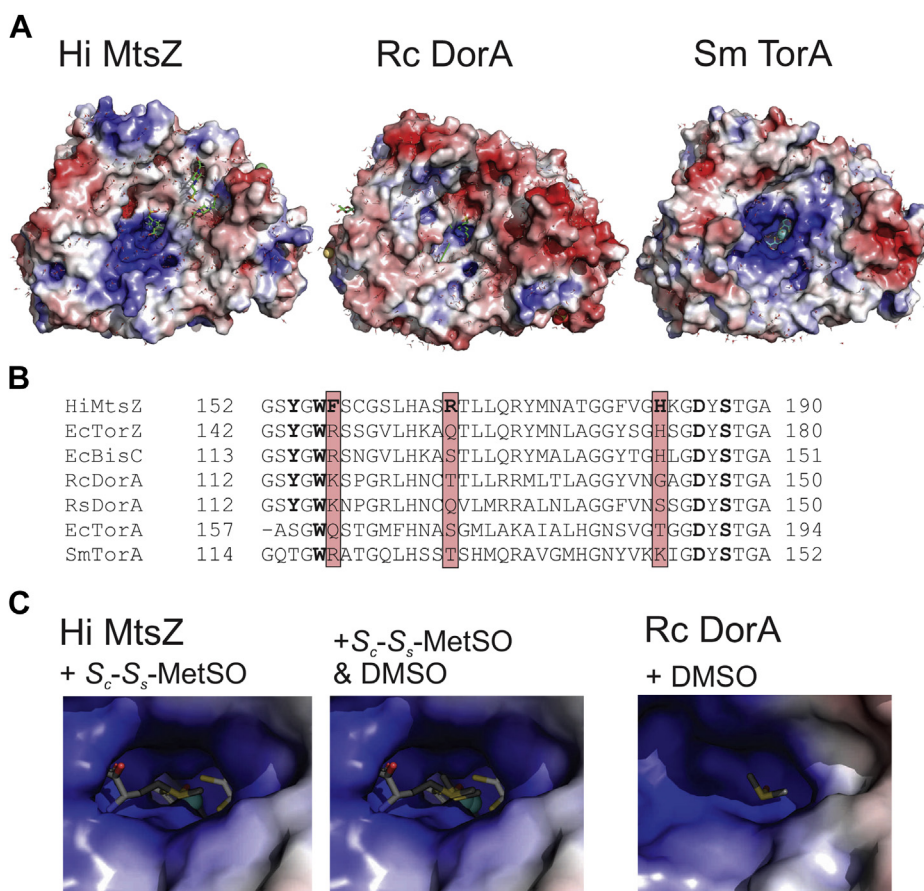


Figure 6. Comparison of electrostatic surface and substrate binding pockets of Dor-/Tor-type S-/N-oxide reductases. *A*, electrostatic surface representation of *Haemophilus influenzae* MtsZ (HiMtsZ), *Rhodobacter capsulatus* DorA (RcDorA), and *Shewanella massilia* TorA (SmTorA). The surface potential is visualized by a color gradient ranging from $-5 k_bT/e_c$ (red) over $0 k_bT/e_c$ (white) to $+5 k_bT/e_c$ (blue). While the overall shape and fold of the three enzymes are remarkably similar, the charged surfaces in the substrate access funnel differ significantly, with predominantly positive charges for HiMtsZ (left) and SmTorA (right), while RcDorA lacks this strong positive charge. In addition, the SmTorA Mo ion is much more solvent-accessible because of the absence of a tyrosine residue (HiMtsZ numbering: Y154). *B*, alignment of residues important for substrate binding in Dor-/Tor-type enzymes. **Bold**, residues important for Mo binding (Ser187), stabilization of serine dissociation stabilization (Asp185), and catalysis (Tyr154, Trp156). **Pink boxes**, residues important for binding of the substrate molecule side chain. HiMtsZ–*Haemophilus influenzae* MtsZ WP_046067646.1; EcTorZ–*Escherichia coli* TorZ WP_000176781.1, EcBisC–*E. coli* BisC WP_000013950.1, RcDorA–*Rhodobacter capsulatus* DorA AAD13674.1, RsDorA–*Rhodobacter sphaeroides* DorA WP_011338998.1, EcTorA–*E. coli* TorA WP_001062091.1, SmTorA–*Shewanella massilia* TorA CAA06851.1, RsBisC–*R. sphaeroides* BisC AAA74739.1. *C*, substrate binding to HiMtsZ and RcDorA. The surface potential is visualized by a color gradient ranging from $-5 k_bT/e_c$ (red) over $0 k_bT/e_c$ (white) to $+5 k_bT/e_c$ (blue). Interactions of substrate molecules (S_c-S_s-MetSO and DMSO) were modeled as described in the [Experimental procedures](#) section; additional data are shown in [Fig. S12](#). BisC, biotin sulfoxide reductases; DMSO, dimethyl sulfoxide; DorA, DorA DMSO reductase; Ec, *Escherichia coli*; HiMtsZ, *Haemophilus influenzae* MtsZ; MetSO, methionine sulfoxide; Rc, *Rhodobacter capsulatus*; Rs, *Rhodobacter sphaeroides*; Sm, *Shewanella massilia*; TorA, TorA TMAO reductase.

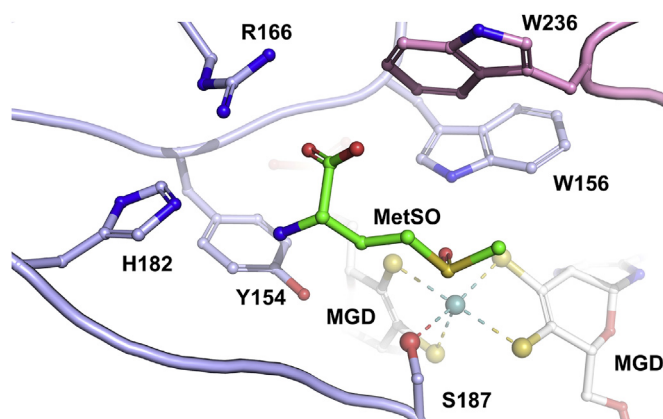


Figure 7. Model of the position of methionine sulfoxide within the HiMtsZ active site. S_c-S_s-MetSO (green); HiMtsZ residues are colored by the structural domain: domain II (pink) and domain III (light blue). HiMtsZ, *Haemophilus influenzae* MtsZ; MetSO, methionine sulfoxide.

Tor-type enzymes, leading to drastic changes in the electrostatic properties of the enzyme surfaces that appear to impact the enzymes' ability to accommodate different S- and N-oxide substrates. Based on this observation, we propose that the substrate-binding sites of all Dor-/Tor-type enzymes are asymmetric. They consist of the previously identified, highly conserved hydrophobic binding pocket that accommodates the central S-/N-oxide moiety, and the larger and highly variable part of the substrate-binding pocket identified here, which appears to be responsible for accommodating the substrate side chain (Fig. 6, Figs. S11 and S12). Our docking experiments also suggest that the known S-sulfoxide specificity of HiMtsZ and other Dor-/Tor-type enzymes (28, 30, 57) is a result of this binding pocket asymmetry that only allows side chains of S-sulfoxides to form the stable interactions between the S-/N lone pair of the substrates and Tyr154 that are required for catalysis in these enzymes (12, 31). Thus, our data indicate that

Molecular basis of molybdenum enzyme diversification

the functional evolution of these enzymes is driven by subtle adjustments of the side chain–coordinating residues in the variable part of the binding pocket.

Discussion

Over the last 3 decades, a deep understanding of the molecular and catalytic properties of Mo enzymes has developed through the integration of structural biology, phylogenetic analysis, coordination chemistry, and spectroscopic studies (19, 25, 43). In the case of the Dor-/Tor-type S-oxide/N-oxide reductases, although it is clear that they form a coherent phylogenetic group with very high structural similarity including at the Mo active site (Figs. S10–S12), the molecular features that lead to their specificity for distinct S-oxides (Table 1) have not previously been identified. Our work provides seminal and compelling insight into the likely structural basis for the increased affinity of HiMtsZ toward its proposed physiological substrate, S_C - S_S -MetSO.

For all three structurally characterized enzymes of this group, DorA, TorA, and HiMtsZ, several conserved tryptophan and tyrosine residues (HiMtsZ: Tyr154, Trp156, Tyr205, Trp236, and Tyr400) dominate the immediate amino acid environment of the Mo active site and form a previously described hydrophobic pocket that accommodates the S-/N-oxide part of the substrate molecules. In this work, we have identified a region with variable surface charge located 10 to 12 Å from the Mo active site that is required to stabilize interactions with substrate side chains. The key residues involved are Arg166 and His182 in HiMtsZ and their equivalent residues in other enzymes (Fig. 6B), where these residues modulate the surface charge and the shape and chemical interactions of the binding surface.

Our data indicate that this second, variable region, which in the case of HiMtsZ, is well adapted to binding S_C - S_S -MetSO, but no other MetSO diastereomer has a significant influence on the catalytic properties of the Dor-/Tor-type enzymes. This is supported by the observation in DorA that the lack of stabilization of the MetSO side chain is reflected in the 50-fold higher K_M for MetSO in this enzyme compared with the more charge-neutral DMSO, whereas turnover numbers for both MetSO and DMSO were essentially the same (31) (Table 1). A similar phenomenon was also reported for RsBisC, where the reported V_{max} values for DMSO, BSO, and MetSO are identical, but BSO had a significantly lower K_M value than the other two substrates (26) (Table 1), and again for EcTorA and two N-oxide substrates with different side chain properties (11). We therefore propose that reduction of S-/N-oxides by Dor-/Tor-type enzymes proceeds with similar efficiencies, while the exact shape and charge of the variable surface area close to the Mo ion determines substrate preferences and K_M values.

The discovery of this highly variable part of the substrate-binding pocket and its significance in Dor-/Tor-type enzyme catalysis has wider implications for the assignment of enzyme function based only on sequence similarities, which is a routine procedure in the analysis of genome sequences. Owing to the high amino acid sequence identity of Dor-/Tor-type

enzymes (average Dor/Tor groups 1 and 2: 49%; group 1: 53%, group 2: 57%), the significance of a variation in only two or three amino acids, such as we have identified here, as determining substrate preferences might very easily be missed in the absence of structural and kinetic studies. This is important, however, as these subtle changes could mean that the catalytic diversity of related enzymes may be much greater than previously assumed. From an evolutionary perspective, substrate availability in a particular niche would be expected to drive selection for specific amino acid sequence variations in the side chain stabilizing part of the substrate-binding pocket. In the case of HiMtsZ, the specificity for S_C - S_S -MetSO enhances the fitness of *H. influenzae* in its human host, where this substrate is naturally available (58). Taken together, our study provides new insights into the evolution of substrate specificity in the Dor/Tor group of S-/N-oxide reductases and its potential to influence niche-specific bacterial fitness and adaptation.

In addition to these insights into the structural basis of substrate preferences, our EPR spectroscopic characterization of the HiMtsZ active site also provides critical insight into the chemical principles that underpin the spectroscopic properties of Mo redox centers. Spectroscopic signatures of Mo enzymes are generally assumed to be influenced by the amino acid environment and the types and number of ligands that coordinate the central Mo atom (48, 59, 60). However, in addition to resembling published EPR signatures of the DorA S-oxide reductase (Table 3, Fig. 2), the form 1 and 2 HiMtsZ EPR spectra were also strikingly similar to those of the Mo-containing NarGH nitrate reductase, which has no significant sequence similarity to HiMtsZ or DorA (Fig. S1) and possesses an aspartate ligand in place of serine. This suggests that the EPR spectroscopic properties of active sites with a MoS_4O_2 first coordination sphere are primarily determined by the presence or absence of a hydroxide ligand, and the orientation of the strongly coupled proton relative to the $4d^1$ redox orbital (43). These structural properties appear to be quite similar in HiMtsZ and NarGH, leading to very similar EPR spectra that are relatively unaffected by the identity of the amino acid ligand (O_{Asp}/O_{Ser}) coordinated to the Mo center. The HiMtsZ EPR studies also provide further evidence for another emerging aspect of Mo enzyme EPR studies, namely the formation of catalytically inactive or ‘off-pathway’ Mo(V) species (48). The HiMtsZ form 1 and form 2 species could not be oxidized to the Mo(VI) state although this is required for catalysis. However, these two forms represent the most dominant EPR signatures for HiMtsZ. In contrast, the likely catalytically active Mo(V) form (form 3) could not only be fully oxidized but also only appeared transiently in EPR redox titrations in a potential range that matched our optical redox titrations of the Mo center.

EPR signatures of molybdenum enzymes have often been used to infer details of their catalytic mechanisms based on the types of ligands coordinated to the Mo ion. Our findings call this into question and clearly indicate that commonly observed EPR signatures do not necessarily originate from catalytically relevant states of the Mo center. A similar observation has most recently been made for the Ec YedY/MsrP enzyme, where initial EPR

spectral titrations also indicated that the Mo center could not be fully oxidized. Subsequent studies showed that the YedY/MsrP EPR spectrum results from an exogenous thiol substituting for the catalytically relevant hydroxide ligand (47, 48), a situation reminiscent of the HiMtsZ form 2 spectrum where glycerol is proposed to displace a hydroxide ligand. It is unclear why some molybdenum enzymes appear to be more prone to forming such off-pathway or inhibited EPR active species, but this may be linked to catalytic plasticity and the existence of alternative pathways of electron flow through the redox centers (61). Thus, additional analyses are required to properly ascertain key links between catalysis and EPR spectroscopic signatures.

Experimental procedures

Standard biochemical methods

Unless otherwise indicated, standard methods were used throughout this study (62). Methyl viologen (MV) chloride, benzyl viologen (BV) chloride, racemic *S/R*-MetSO (*rac*-MetSO), and *S*-methionine-*R/S*-sulfoxide (*S_C-RS_S-MetSO*) (63), a mixture of four and two stereoisomers, respectively, (Scheme S1), TMAO, as well as all other *S*- and *N*-oxides (Scheme S1) used were purchased from Merck or Sigma-Aldrich and used as received. The BSO diastereomers *S*-BSO and *R*-BSO were prepared as previously reported (64, 65). All solutions were prepared with ultrapure water (resistivity 18.2 MΩ cm) from a Millipore Milli-Q system. Protein concentrations were determined using a BCA-1 Assay Kit (Sigma). SDS-PAGE used the protocol of Laemmli (66); LMW SDS-PAGE Ladder (Cytiva) was used as the molecular mass standard.

Production and purification of recombinant HiMtsZ

Recombinant 6-His-tagged HiMtsZ was expressed in *Ec* DH5α containing pProex-HiTorZ-sp, as described (4). Expression cultures used LB supplemented with 100 μg/ml ampicillin and 1 mM sodium molybdate. Protein expression was induced by the addition of 100 μM IPTG at an absorbance at 600 nm of ~0.8, followed by overnight incubation at 30 °C. Preparation of cell extracts and protein purification were essentially carried out as reported (4), using a combination of immobilized metal affinity chromatography and size-exclusion chromatography, but with the omission of glycerol from the final storage buffer (20 mM Tris Cl, pH 8.0). Fractions were analyzed by SDS-PAGE throughout, pooled according to their purity, and desalted into storage buffer using PD10 columns (Cytiva) before storage at -80 °C.

Crystallization

Purified recombinant HiMtsZ was concentrated to ~9 mg/ml for screening of crystallization conditions. Screens were set up at the UQ Remote Operation Crystallization and X-ray Diffraction (UQROCX) facility by hanging-drop vapor diffusion with a Mosquito (TTP Labtech) pipetting robot and commercial screening reagent sets: HR2-144, HR2-126, HR2-098, HR2-082, HR2-084, HR2-247, HR2-211, HR2-219, and HR2-217 (Hampton Research) and MD1-88, MD1-29, and MD1-38 (Molecular Dimensions). The initial hit (Screen HR2-

084/PEGRx 2 reagent 25: 100 mM citrate buffer, pH 5.5, 22% PEG 3350, 0.10% w/v *n*-octyl-β-*D*-glucoside) was reproduced and conditions refined (changes: detergent and PEG concentrations; temperature and inclusion of MetSO) in 24-well plates by hanging-drop vapor diffusion with 2-μl-sized drops. The final crystallization conditions were 100 mM Na-citrate buffer, 100 mM MetSO, 22% PEG 3350, pH 5.5, for acidic conditions and 100 mM Hepes, 22% PEG 3350, pH 7.0, for neutral conditions.

Data collection and processing

Crystals were mounted onto CryoLoops (Hampton Research) and immediately soaked in Paratone-N (Hampton Research) for 30 s before flash-cooling in liquid nitrogen. Diffraction data were acquired at the Australian Synchrotron MX-2 beamline *via* remote control with an EIGER 2 9M detector (Dectris) at 100 K. The X-ray energy was 13,000 eV, and the rotation angle was 180°. Image files were indexed and integrated using XDS (67), scaled, and merged with Aimless (CCP4 suite). Phasing was achieved by molecular replacement using the BALBES pipeline (68). For density modification and model building, AutoBuild (69) was used and *phenix.refine* (70) for structure refinement. Ligand restraints for the Mo-PGD ligands were generated using eLBOW (71). In the pH 7.0 MtsZ crystal structure, the coordinates for the terminal water-based ligand with 80% occupancy were restrained to the peak of the electron density. The PGD ligands, the molybdenum atom, and the water-based ligand were fit into the electron density using the COOT (72) interface. Manual corrections were also performed through COOT. For validation, composite omit maps were generated with *phenix.composite_omit_map* using simulated annealing to remove model bias (73). Molecular graphics presented in this work were created with PyMOL (Schrödinger). Electron densities are shown as composite omit maps contoured at 1 σ. The structure of HiMtsZ was compared with other structures using Dali (74, 75). Docking of potential HiMtsZ substrates to the active site for identification of residues important for substrate specificity was performed with Glide in the extra-precision mode (76) through the Maestro interface (Schrödinger). Briefly, the protein and potential substrates were processed for docking using the Protein Preparation Wizard and LigPrep (77). States for the receptor were generated at pH 7.5 and states for the substrates for pH 7.4 ± 2.0. For the receptor grid, a 20 × 20 × 20 Å cubicle surrounding the active site was defined. A metal constraint to the Mo ion and postdocking energy minimization were incorporated into the docking protocol. Homology models of *Ec* BisC (WP_000013950.1) and TorZ (WP_000176781.1) were built using Prime (Schrödinger) with HiMtsZ as the template. Electrostatic surface representations were generated using Adaptive Poisson-Boltzmann Solver (78) after preprocessing the models through PDB2PQR (79). The numbering of the residues in the HiMtsZ structure follows the amino acid numbers of unprocessed HiMtsZ WT protein (consistent with the gene sequence). We note that the numbering for residues in crystal structures of other Dor/Tor enzymes in the literature is often based on the mature,

Molecular basis of molybdenum enzyme diversification

processed protein that lacks the signal peptide required for export of the protein to the periplasm (14, 21). As a result, the residue numbers in these different crystal structures differ by ~ 30 amino acids.

S- and N-oxide reductase activity assays

MtsZ S- and N-oxide reductase activity was determined using a methyl-viologen-based enzyme assay, as reported previously (4). Assays were performed anaerobically at 37 °C and contained 0.2 mM MV²⁺ and 0.3 mM sodium dithionite in 20 mM Tris Cl, pH 8.0. Standard assays contained 10 mM DMSO or MetSO; all other substrates were used in concentrations up to 10 mM. Buffers for analysis of HiMtsZ activity pH dependence contained 20 mM sodium dihydrogen phosphate, 20 mM Tris base, and 20 mM glycine and were titrated with sodium hydroxide or hydrochloric acid; assays for the pH dependence of the MtsZ reaction used 10 mM *S_C-RS_S-MetSO* as the substrate. Absorbance changes were monitored over time at 600 nm using a Cary 60 spectrophotometer (Varian). For calculation of S-/N-oxide reductase activity, an extinction coefficient of 13.7 mM⁻¹ cm⁻¹ for MV²⁺ was used (80). Direct nonlinear data fitting to the Michaelis–Menten equation was performed with Prism 8.0 (GraphPad).

Electrochemical measurements and enzyme electrode preparation

CV determines the potential-dependent catalytic current between the catalyst tested and an electrode. At potential values where catalysis is effective, a strong increase in the current is normally observed. Each measurement consists of forward and reverse sweeps of the potential range used, and typically, these sweeps do not yield identical profiles. CV experiments were carried out with a BAS 100B/W electrochemical workstation and a three-electrode system comprising a GC disk working electrode, a Pt wire counter, and an Ag/AgCl reference electrode (+196 mV *versus* NHE). Experiments used 50 mM Tris Cl, pH 8.0, that had been purged with Ar gas for at least 30 min, and an Ar blanket was maintained during the measurement. GC electrodes were polished with 0.50 and 0.05 μm alumina slurries, rinsed thoroughly with water, and sonicated in water for 5 min to remove any adsorbed alumina particles, before drying in a nitrogen atmosphere. A 3-μl droplet of HiMtsZ (15 μM) was pipetted onto the conducting surface of an inverted, freshly cleaned GC working electrode and allowed to evaporate to a film at 4 °C. To prevent protein loss, the electrode was then carefully covered with a presoaked dialysis membrane (molecular weight cut-off 3500 Da), confining HiMtsZ under the membrane while allowing diffusion of the mediator, substrate, and product molecules. The dialysis membrane was fastened to the electrode with the help of a Teflon cap and a rubber O-ring. The resulting GC/MtsZ electrode was stored at 4 °C in 50 mM Tris Cl (pH 8.0) when not in use. Electrochemically driven catalysis of HiMtsZ was pursued using the mediators MV²⁺ and BV²⁺ and S- and N-oxide substrates as indicated. The variation of the observed limiting catalytic current (i_{lim}) as a function of the substrate

concentration followed Michaelis–Menten kinetics, and the data were fit to Equation 1.

$$i_{lim} = \frac{i_{max}[Substrate]}{K_{M,app} + [Substrate]} \quad (1)$$

Where i_{max} is the catalytic current at saturation and $K_{M,app}$ is the apparent Michaelis constant.

In all cases, *rac*MetSO was used as the substrate (Scheme S1). No attempt was made to separate this mixture or establish which isomer was the most reactive.

Protein spectroelectrochemistry

Spectroelectrochemistry determines changes in the UV/Vis absorption spectrum of redox-active components in proteins as a function of the redox potential of the working solution. Experiments were conducted with a Pine Instruments quartz spectroelectrochemical cell (1.7-mm optical path length) using a Pt 'honeycomb' working electrode, a Pt auxiliary electrode, and an Ag/AgCl reference electrode. The cell contained 200 μM HiMtsZ in Tris Cl buffer (50 mM, pH 8.0). To ensure efficient electrochemical communication, the mediators [Fe(tacn)₂]³⁺, [Fe(*trans*-diammac)]³⁺, [Co(NMe₃MEN₃S₃sar)]⁴⁺, and [Co(AMMEN₄S₂sar)]³⁺ were present each at a concentration of 20 μM; the structures and properties of these compounds have been published (81–83). These mediators span the oxidation-reduction potential range +200 to –200 mV *versus* NHE and have small molar extinction coefficients, so they make little contribution to the visible spectra at micromolar concentrations. They have no absorbance at wavelengths longer than 600 nm, which was the region of interest here. Spectra were acquired within an anaerobic glovebox with an Ocean Optics USB2000 fiber-optic spectrophotometer and a DT-MINI-2-GS miniature deuterium/tungsten/halogen UV-Vis-NIR light source. Potentials were set with a BAS100B/W potentiostat operating in a constant potential chronocoulometry mode, and UV-Vis spectra were taken when equilibrium was established and all absorbance changes ceased. Spectra were acquired at 50 mV intervals, and reversibility was established by stepping the potential firstly in negative and then in positive directions. No significant hysteresis was found. Data were modeled with ReactLab Redox (Ver. 1.1, J Plus Consulting Pty Ltd) using a sequential two-electron transfer model, which afforded the Mo^{VI/V} and Mo^{V/IV} redox potentials as well as the spectra of the fully oxidized (Mo^{VI}), single-electron-reduced (Mo^V) and fully reduced (Mo^{IV}) forms.

EPR spectroscopy

EPR spectroscopy is used to study the electronic interactions between atoms surrounding, for example, a metal center, such as the HiMtsZ Mo active site. To generate an EPR signal, redox centers must contain unpaired electrons; the shape of the signal depends on orbital interactions between the metal center and the surrounding atoms. Continuous-wave X-band (ca. 9.385 GHz) EPR spectra were recorded on a Bruker ElexSys E540 spectrometer equipped

with an ElexSys Super High Sensitivity Probe head and LN₂ cooling (Eurotherm temperature control). The magnetic field was calibrated with 2,2-diphenyl-1-picrylhydrazyl ($g = 2.0036$), and measurements were carried out at 135 K using a modulation amplitude of 0.5 mT, a modulation frequency of 100 kHz, and a microwave power of 5.024 mW (16 dB of 200 mW, nonsaturating condition). EPR samples used 50 μ M HiMtsZ. The following redox mediators were present each at a concentration of 40 μ M: dichlorophenolindophenol, 1,2-naphthoquinone-4-sulfonate, 2-hydroxynaphthoquinone, 2,6-dimethylbenzoquinone, 2,5-dihydroxybenzoquinone, anthraquinone-2-sulfonate, and BV. The reductant was sodium dithionite and the oxidant potassium ferricyanide (ca. 1 mM solutions).

Computational studies and EPR spectral simulations

Ground-state geometry optimizations were performed at the density functional level of theory using the ORCA suite (version 4.1.0) (84). The B3LYP hybrid functional and a def2-TZVP basis set were used in these calculations with the RIJ-COSX approximation. These optimized geometries were then used to compute the spin-Hamiltonian parameters. The zero-order regular approximation (ZORA) (85, 86) was turned on for these calculations. For the EPR calculations, Old-ZORA-TZVPP, ZORA-def2-TZVPP, and ZORA-def2-TZVP basis sets were used for the Mo atom, S atoms, and the light atoms, respectively. Experimental EPR spin-Hamiltonian parameters were obtained from spectral simulations performed using the EasySpin suite (version 5.2.28) (87), which is embedded within the MATLAB (version 9.8.0.1359463) (R2020a) platform. A multicomponent EPR model was used to fit EPR spectra with nonlinear parameter optimization (g -values, hyperfine couplings, and linewidths) carried out using a Newton–Gauss–Levenberg/Marquardt algorithm and the linear parameters (component intensities) computed using linear least-squares with the constraint that the component intensities are non-negative. This was achieved with the 'lsqnonneg' function in MATLAB.

Data availability

The crystal structures of HiMtsZ, pH 5.5 and pH 7.0, have been deposited with the Protein Data Bank (PDB) under accession numbers 7L5I (pH 7.0 MtsZ structure) and 7L5S (pH 5.5 MtsZ structure) (to be released on acceptance of the article). Homology models of *Escherichia coli* BisC and TorZ are available as part of the supplementary material. All remaining data are contained within the article.

Supporting information—This article contains [supporting information](#).

Acknowledgments—We acknowledge the use of the University of Queensland Remote Operation Crystallization and X-ray (UQROCX) Facility at the Centre for Microscopy and Microanalysis and the support from staff, Gordon King and Karl Byriel. We also

acknowledge use of the Australian Synchrotron MX facility and thank the staff for their support.

Author contributions—M. A. S. prepared recombinant protein for all analyses mentioned in the article and carried out the majority of the structural work. P. K. and P. V. B. carried out the electrochemical activity analyses, and Z. L. and B. K. directed the protein structure analyses. Q. Z. and U. K. carried out phylogenetic analyses, U. K., D. E., and Q. Z. carried out the optical MtsZ activity assays. J. Y., K. C. K., J. R. H., M. L. K., and P. V. B. carried out the collection and analysis of HiMtsZ EPR data, and A. G. M. and B. C. provided critical evaluations. U. K. was responsible for the project concept and design, supervision of Q. Z. and M. A. S. (together with B. K.), and the drafting and editing of the manuscript. All authors contributed to the writing of the manuscript.

Funding and additional information—This work was supported by Australian Research Council Discovery Grant DP190103158 to P. V. B., National Health and Medical Research Council Project Grant GNT1158451 to U. K. and A. G. M., and National Health and Medical Research Council Ideas Grant 1180826 to B. K. B. K. is an Australian Research Council Laureate Fellow (FL180100109). M. L. K. acknowledges the National Institutes of Health (R01-GM-057378) for continued financial support. M. A. S. is a recipient of a scholarship funded by the Studienstiftung des Deutschen Volkes and received a travel grant from the Bayer Science and Education Foundation. The content is solely the responsibility of the authors and does not necessarily represent the official views of the National Institutes of Health.

Conflict of interest—The authors declare that they have no conflicts of interest with the contents of this article.

Abbreviations—The abbreviations used are: BisC, biotin sulfoxide reductases; BSO, biotin sulfoxide; BV, benzyl viologen; CV, cyclic voltammetry; DMSO, dimethyl sulfoxide; DorA, DorA DMSO reductase; Ec, *Escherichia coli*; EPR, electron paramagnetic resonance; GC, glassy carbon; Hi, *Haemophilus influenzae*; HiMtsZ, methionine sulfoxide reductase from *Haemophilus influenzae*; *lpH*, low pH; MetSO, methionine sulfoxide; MPTSO, methyl *p*-tolyl sulfoxide; MV, methyl viologen; NarGH, NarGH dissimilatory nitrate reductase; NHE, normal hydrogen electrode; PGD, pyranopterin guanine dinucleotide; *rac*MetSO, racemic methionine sulfoxide; Rc, *Rhodobacter capsulatus*; Rs, *Rhodobacter sphaeroides*; Sm, *Shewanella massilia*; TMAO, trimethylamine N-oxide; TorA, TorA TMAO reductase; ZORA, zero-order regular approximation.

References

- Kappler, U., and Schaefer, H. (2014) Conversions of dimethylsulfide. In: Kroneck, P. M. H., Sosa Torres, M., eds. *The Metal-Driven Biogeochemistry of Gaseous Compounds in the Environment*, Springer International Publishing AG, Cham, Switzerland: 279–313
- Larosa, V., and Remacle, C. (2018) Insights into the respiratory chain and oxidative stress. *Biosci. Rep.* **38**, BSR20171492
- Hawkins, C. L., Pattison, D. I., and Davies, M. J. (2003) Hypochlorite-induced oxidation of amino acids, peptides and proteins. *Amino Acids* **25**, 259–274
- Dhouib, R., Othman, D. S. M. P., Lin, V., Lai, X. J., Wijesinghe, H. G. S., Essilfie, A.-T., Davis, A., Nasreen, M., Bernhardt, P. V., Hansbro, P. M., McEwan, A. G., and Kappler, U. (2016) A novel, molybdenum-containing

Molecular basis of molybdenum enzyme diversification

- methionine sulfoxide reductase supports survival of *Haemophilus influenzae* in an *in vivo* model of infection. *Front. Microbiol.* **7**, e1743
- Eldere, J. V., Slack, M. P. E., Ladhani, S., and Cripps, A. W. (2014) Non-typeable *Haemophilus influenzae*, an under-recognised pathogen. *Lancet Infect. Dis.* **14**, 1281–1292
 - Wootton, D. G., Cox, M. J., Gloor, G. B., Litt, D., Hoschler, K., German, E., Court, J., Eneje, O., Keogan, L., Macfarlane, L., Wilks, S., Diggle, P. J., Woodhead, M., Moffatt, M. F., Cookson, W. O. C., et al. (2019) A *Haemophilus* sp. dominates the microbiota of sputum from UK adults with non-severe community acquired pneumonia and chronic lung disease. *Sci. Rep.* **9**, 2388
 - King, P. (2012) *Haemophilus influenzae* and the lung (*Haemophilus* and the lung). *Clin. Transl. Med.* **1**, 10
 - Román, F., Cantón, R., Pérez-Vázquez, M., Baquero, F., and Campos, J. (2004) Dynamics of long-term colonization of respiratory tract by *Haemophilus influenzae* in cystic fibrosis patients shows a marked increase in hypermutable strains. *J. Clin. Microbiol.* **42**, 1450–1459
 - Lansbury, L., Lim, B., Baskaran, V., and Lim, W. S. (2020) Co-infections in people with COVID-19: A systematic review and meta-analysis. *J. Infect.* **81**, 266–275
 - Czjzek, M., DosSantos, J. P., Pommier, J., Giordano, G., Mejean, V., and Haser, R. (1998) Crystal structure of oxidized trimethylamine N-oxide reductase from *Shewanella massilia* at 2.5 Å resolution. *J. Mol. Biol.* **284**, 435–447
 - Iobbi-Nivol, C., Pommier, J., Simala-Grant, J., Mejean, V., and Giordano, G. (1996) High substrate specificity and induction characteristics of trimethylamine-N-oxide reductase of *Escherichia coli*. *Biochim. Biophys. Acta* **1294**, 77–82
 - Ridge, J. P., Aguey-Zinsou, K. F., Bernhardt, P. V., Brereton, I. M., Hanson, G. R., and McEwan, A. G. (2002) Site-directed mutagenesis of dimethyl sulfoxide reductase from *Rhodobacter capsulatus*: Characterization of a Y114 → F mutant. *Biochemistry* **41**, 15762–15769
 - Hilton, J. C., Temple, C. A., and Rajagopalan, K. V. (1999) Re-design of *Rhodobacter sphaeroides* dimethyl sulfoxide reductase. *J. Biol. Chem.* **274**, 8428–8436
 - McAlpine, A. S., McEwan, A. G., Shaw, A. L., and Bailey, S. (1997) Molybdenum active centre of DMSO reductase from *Rhodobacter capsulatus*: Crystal structure of the oxidised enzyme at 1.82-Å resolution and the dithionite-reduced enzyme at 2.8-Å resolution. *J. Biol. Inorg. Chem.* **2**, 690–701
 - Zhong, Q., Kobe, B., and Kappler, U. (2020) Molybdenum enzymes and how they support virulence in pathogenic bacteria. *Front. Microbiol.* **11**, 615860
 - Miralles-Robledillo, J. M., Torregrosa-Crespo, J., Martínez-Espinosa, R. M., and Pire, C. (2019) DMSO reductase family: Phylogenetics and applications of extremophiles. *Int. J. Mol. Sci.* **20**, 3349
 - Kappler, U., Nasreen, M., and McEwan, A. (2019) New insights into the molecular physiology of sulfoxide reduction in bacteria. *Adv. Microb. Physiol.* **75**, 1–51
 - Rothery, R. A., Workun, G. J., and Weiner, J. H. (2008) The prokaryotic complex iron-sulfur molybdoenzyme family. *Biochim. Biophys. Acta* **1778**, 1897–1929
 - Hille, R., Hall, J., and Basu, P. (2014) The mononuclear molybdenum enzymes. *Chem. Rev.* **114**, 3963–4038
 - Schindelin, H., Kisker, C., Hilton, J., Rajagopalan, K. V., and Rees, D. C. (1996) Crystal structure of DMSO reductase: Redox-linked changes in molybdopterin coordination. *Science* **272**, 1615–1621
 - Schneider, F., Loewe, J., Huber, R., Schindelin, H., Kisker, C., and Knaeblein, J. (1996) Crystal structure of dimethyl sulfoxide reductase from *Rhodobacter capsulatus* at 1.88 Å resolution. *J. Mol. Biol.* **263**, 53–69
 - Bastian, N. R., Kay, C. J., Barber, M. J., and Rajagopalan, K. V. (1991) Spectroscopic studies of the molybdenum-containing DMSO reductase from *Rhodobacter sphaeroides* f. sp. denitrificans. *J. Biol. Chem.* **266**, 45–51
 - Bennett, B., Benson, N., McEwan, A. G., and Bray, R. C. (1994) Multiple states of the molybdenum centre of dimethylsulphoxide reductase from *Rhodobacter capsulatus* revealed by EPR spectroscopy. *Eur. J. Biochem.* **225**, 321–331
 - George, G. N., Hilton, J., and Rajagopalan, K. V. (1996) X-Ray absorption spectroscopy of dimethyl sulfoxide reductase from *Rhodobacter sphaeroides*. *J. Am. Chem. Soc.* **118**, 1113–1117
 - Mtei, R. P., Lyashenko, G., Stein, B., Rubie, N., Hille, R., and Kirk, M. L. (2011) Spectroscopic and electronic structure studies of a dimethyl sulfoxide reductase catalytic intermediate: Implications for electron- and atom-transfer reactivity. *J. Am. Chem. Soc.* **133**, 9762–9774
 - Pollock, V. V., and Barber, M. J. (1997) Biotin sulfoxide reductase | heterologous expression and characterization of a functional molybdopterin guanine dinucleotide-containing enzyme. *J. Biol. Chem.* **272**, 3355–3362
 - Temple, C. A., George, G. N., Hilton, J. C., George, M. J., Prince, R. C., Barber, M. J., and Rajagopalan, K. V. (2000) Structure of the molybdenum site of *Rhodobacter sphaeroides* biotin sulfoxide reductase. *Biochemistry* **39**, 4046–4052
 - Ezraty, B., Bos, J., Barras, F., and Aussel, L. (2005) Methionine sulfoxide reduction and assimilation in *Escherichia coli*: New role for the biotin sulfoxide reductase BisC. *J. Bacteriol.* **187**, 231–237
 - Gon, S., Patte, J. C., Mejean, V., and Iobbi-Nivol, C. (2000) The *torYZ* (*yecK-bisZ*) operon encodes a third respiratory trimethylamine N-oxide reductase in *Escherichia coli*. *J. Bacteriol.* **182**, 5779–5786
 - Denkel, L. A., Rhen, M., and Bange, F.-C. (2013) Biotin sulfoxide reductase contributes to oxidative stress tolerance and virulence in *Salmonella enterica* serovar *Typhimurium*. *Microbiol.* **159**, 1447–1458
 - Johnson, K. E., and Rajagopalan, K. V. (2001) An active site tyrosine influences the ability of the dimethyl sulfoxide reductase family of molybdopterin enzymes to reduce S-oxides. *J. Biol. Chem.* **276**, 13178–13185
 - Adams, B., Smith, A. T., Bailey, S., McEwan, A. G., and Bray, R. C. (1999) Reactions of dimethylsulfoxide reductase from *Rhodobacter capsulatus* with dimethyl sulfide and with dimethyl sulfoxide: Complexities revealed by conventional and stopped-flow spectrophotometry. *Biochemistry* **38**, 8501–8511
 - Pollock, V. V., and Barber, M. J. (1995) Molecular cloning and expression of biotin sulfoxide reductase from *Rhodobacter sphaeroides* forma sp. *denitrificans*. *Arch. Biochem. Biophys.* **318**, 322–332
 - Kappler, U., and Bailey, S. (2005) Molecular basis of intramolecular electron transfer in sulfite-oxidizing enzymes is revealed by high resolution structure of a heterodimeric complex of the catalytic molybdopterin subunit and a c-type cytochrome subunit. *J. Biol. Chem.* **280**, 24999–25007
 - Li, H. K., Temple, C., Rajagopalan, K. V., and Schindelin, H. (2000) The 1.3 Å crystal structure of *Rhodobacter sphaeroides* dimethyl sulfoxide reductase reveals two distinct molybdenum coordination environments. *J. Am. Chem. Soc.* **122**, 7673–7680
 - Rothery, R. A., Stein, B., Solomonson, M., Kirk, M. L., and Weiner, J. H. (2012) Pyranopterin conformation defines the function of molybdenum and tungsten enzymes. *Proc. Natl. Acad. Sci. U. S. A.* **109**, 14773–14778
 - Loschi, L., Brokx, S. J., Hills, T. L., Zhang, G., Bertero, M. G., Lovering, A. L., Weiner, J. H., and Strynadka, N. C. (2004) Structural and biochemical identification of a novel bacterial oxidoreductase. *J. Biol. Chem.* **279**, 50391–50400
 - Gennaris, A., Ezraty, B., Henry, C., Agrebi, R., Vergnes, A., Oheix, E., Bos, J., Leverrier, P., Espinosa, L., Szweczyk, J., Vertommen, D., Iranzo, O., Collet, J.-F., and Barras, F. (2015) Repairing oxidized proteins in the bacterial envelope using respiratory chain electrons. *Nature* **528**, 409–412
 - McEwan, A. G., Ferguson, S. J., and Jackson, J. B. (1991) Purification and properties of DMSO reductase from *Rhodobacter capsulatus*: A periplasmic molybdoenzyme. *Biochem. J.* **274**, 305–308
 - Finnegan, M. G., Hilton, J., Rajagopalan, K. V., and Johnson, M. K. (1993) Optical transitions of molybdenum(V) in glycerol-inhibited DMSO reductase from *Rhodobacter sphaeroides*. *Inorg. Chem.* **32**, 2616–2617
 - Cobb, N., Conrads, T., and Hille, R. (2005) Mechanistic studies of *Rhodobacter sphaeroides* Me₂SO reductase. *J. Biol. Chem.* **280**, 11007–11017
 - George, G. N., Hilton, J., Temple, C., Prince, R. C., and Rajagopalan, K. V. (1999) Structure of the molybdenum site of dimethyl sulfoxide reductase. *J. Am. Chem. Soc.* **121**, 1256–1266
 - Rendon, J., Biaso, F., Ceccaldi, P., Toci, R., Seduk, F., Magalon, A., Guigliarelli, B., and Grimaldi, S. (2017) Elucidating the structures of the low- and high-pH Mo(V) species in respiratory nitrate reductase: A combined EPR, 14,15N HYSCORE, and DFT study. *Inorg. Chem.* **56**, 4422–4434
 - Vincent, S. P., and Bray, R. C. (1978) Electron-paramagnetic-resonance studies on nitrate reductase from *Escherichia coli* K12. *Biochem. J.* **171**, 639–647

45. Enemark, J. H., Astashkin, A. V., and Raitsimring, A. M. (2006) Investigation of the coordination structures of the molybdenum(V) sites of sulfite oxidizing enzymes by pulsed EPR spectroscopy. *Dalton Trans.* 3501–3514
46. Magalon, A., Asso, M., Guigliarelli, B., Rothery, R. A., Bertrand, P., Giordano, G., and Blasco, F. (1998) Molybdenum cofactor properties and [Fe-S] cluster coordination in *Escherichia coli* nitrate reductase A: Investigation by site-directed mutagenesis of the conserved His-50 residue in the NarG subunit. *Biochemistry* **37**, 7363–7370
47. Brox, S. J., Rothery, R. A., Zhang, G., Ng, D. P., and Weiner, J. H. (2005) Characterization of an *Escherichia coli* sulfite oxidase homologue reveals the role of a conserved active site cysteine in assembly and function. *Biochemistry* **44**, 10339–10348
48. Ingersol, L. J., Yang, J., Kc, K., Pokhrel, A., Astashkin, A. V., Weiner, J. H., Johnston, C. A., and Kirk, M. L. (2020) Addressing ligand-based redox in molybdenum-dependent methionine sulfoxide reductase. *J. Am. Chem. Soc.* **142**, 2721–2725
49. Benson, N., Farrar, J. A., McEwan, A. G., and Thomson, A. J. (1992) Detection of the optical bands of molybdenum(V) in DMSO reductase (*Rhodobacter capsulatus*) by low-temperature MCD spectroscopy. *FEBS Lett.* **307**, 169–172
50. Bard, A. J., and Faulkner, L. R. (2001) *Electrochemical Methods: Fundamentals and Applications*, Wiley & Sons Inc, New York, NY
51. Kalimuthu, P., Heider, J., Knack, D., and Bernhardt, P. V. (2015) Electrocatalytic hydrocarbon hydroxylation by ethylbenzene dehydrogenase from *Aromatoleum aromaticum*. *J. Phys. Chem. B* **119**, 3456–3463
52. Kalimuthu, P., Belaidi, A. A., Schwarz, G., and Bernhardt, P. V. (2017) Mediated catalytic voltammetry of holo and heme-free human sulfite oxidases. *ChemElectroChem* **4**, 947–956
53. Kalimuthu, P., Heath, M. D., Santini, J. M., Kappler, U., and Bernhardt, P. V. (2014) Electrochemically driven catalysis of *Rhizobium sp.* NT-26 arsenite oxidase with its native electron acceptor cytochrome c552. *Biochim. Biophys. Acta* **1837**, 112–120
54. Maia, L. B., Fonseca, L., Moura, I., and Moura, J. J. G. (2016) Reduction of carbon dioxide by a molybdenum-containing formate dehydrogenase: A kinetic and mechanistic study. *J. Am. Chem. Soc.* **138**, 8834–8846
55. Pollock, V. V., and Barber, M. J. (2000) Serine 121 is an essential amino acid for biotin sulfoxide reductase functionality. *J. Biol. Chem.* **275**, 35086–35090
56. Kaufmann, P., Duffus, B. R., Mitrova, B., Iobbi-Nivol, C., Teutloff, C., Nimtz, M., Jansch, L., Wollenberger, U., and Leimkühler, S. (2018) Modulating the molybdenum coordination sphere of *Escherichia coli* trimethylamine N-oxide reductase. *Biochemistry* **57**, 1130–1143
57. Abo, M., Tachibana, M., Okubo, A., and Yamazaki, S. (1994) Enantioselective reduction of the sulfoxide to sulfide in methyl phenyl sulfoxide by dimethyl sulfoxide reductase from *Rhodobacter sphaeroides f. s. denitrificans*. *Biosci. Biotechnol. Biochem.* **58**, 596–597
58. Farne, H., Groves, H. T., Gill, S. K., Stokes, I., McCulloch, S., Karoly, E., Trujillo-Torralbo, M.-B., Johnston, S. L., Mallia, P., and Tregoning, J. S. (2018) Comparative metabolomic sampling of upper and lower airways by four different methods to identify biochemicals that may support bacterial growth. *Front. Cell. Infect. Microbiol.* **8**, 432
59. Khananand, K. C., and Kirk, M. L. (2020) Molybdenum and tungsten cofactors and the reactions they catalyze. *Met. Ions Life Sci.* <https://doi.org/10.1515/9783110589757-015>
60. Kirk, M. L. (2017) Chapter 2 spectroscopic and electronic structure studies of Mo model compounds and enzymes. In: Hille, R., Schulzke, C., Kirk, M. L., eds. *Molybdenum and Tungsten Enzymes: Spectroscopic and Theoretical Investigations*, The Royal Society of Chemistry, London: 13–67
61. Emesh, S., Rapson, T. D., Rajapaksha, A., Kappler, U., Bernhardt, P. V., Tollin, G., and Enemark, J. H. (2009) Intramolecular electron transfer in sulfite-oxidizing enzymes: Elucidating the role of a conserved active site arginine. *Biochemistry* **48**, 2156–2163
62. Ausubel, F. M., Brent, R., Kingston, R. E., Moore, D. D., Seidman, J. G., Smith, J. A., and Struhl, K. (2003) *Current Protocols in Molecular Biology* (Vol 2003). John Wiley & Sons, Inc, New York, NY
63. Bentley, R. (2005) Methionine and derivatives: Exploring chirality at sulfur. *Biochem. Mol. Biol. Educ.* **33**, 274–276
64. Melville, D. B. (1954) Biotin sulfoxide. *J. Biol. Chem.* **208**, 495–501
65. Melville, D. B., Genghof, D. S., and Lee, J. M. (1954) Biological properties of biotin d- and l-sulfoxides. *J. Biol. Chem.* **208**, 503–512
66. Laemmli, U. (1970) Cleavage of structural proteins during the assembly of the head of bacteriophage T4. *Nature* **227**, 680–685
67. Kabsch, W. (2010) Xds. *Acta Crystallogr. D Biol. Crystallogr.* **66**, 125–132
68. Long, F., Vagin, A. A., Young, P., and Murshudov, G. N. (2008) Balbes: A molecular-replacement pipeline. *Acta Crystallogr. D Biol. Crystallogr.* **64**, 125–132
69. Terwilliger, T. C., Grosse-Kunstleve, R. W., Afonine, P. V., Moriarty, N. W., Zwart, P. H., Hung, L. W., Read, R. J., and Adams, P. D. (2008) Iterative model building, structure refinement and density modification with the PHENIX AutoBuild wizard. *Acta Crystallogr. D Biol. Crystallogr.* **64**, 61–69
70. Afonine, P. V., Grosse-Kunstleve, R. W., Echols, N., Headd, J. J., Moriarty, N. W., Mustyakimov, M., Terwilliger, T. C., Urzhumtsev, A., Zwart, P. H., and Adams, P. D. (2012) Towards automated crystallographic structure refinement with phenix.refine. *Acta Crystallogr. D Biol. Crystallogr.* **68**, 352–367
71. Moriarty, N. W., Grosse-Kunstleve, R. W., and Adams, P. D. (2009) Electronic ligand builder and optimization workbench (eLBOW): A tool for ligand coordinate and restraint generation. *Acta Crystallogr. D Biol. Crystallogr.* **65**, 1074–1080
72. Emsley, P., Lohkamp, B., Scott, W. G., and Cowtan, K. (2010) Features and development of Coot. *Acta Crystallogr. D Biol. Crystallogr.* **66**, 486–501
73. Terwilliger, T. C., Grosse-Kunstleve, R. W., Afonine, P. V., Moriarty, N. W., Adams, P. D., Read, R. J., Zwart, P. H., and Hung, L. W. (2008) Iterative-build OMIT maps: Map improvement by iterative model building and refinement without model bias. *Acta Crystallogr. D Biol. Crystallogr.* **64**, 515–524
74. Holm, L., Käriäinen, S., Wilton, C., and Plewczynski, D. (2006) Using Dali for structural comparison of proteins. *Curr. Protoc. Bioinformatics*
75. Holm, L., and Laakso, L. M. (2016) Dali server update. *Nucleic Acids Res.* **44**, W351–W355
76. Friesner, R. A., Murphy, R. B., Repasky, M. P., Frye, L. L., Greenwood, J. R., Halgren, T. A., Sanschagrin, P. C., and Mainz, D. T. (2006) Extra precision glide: Docking and scoring incorporating a model of hydrophobic enclosure for protein-ligand complexes. *J. Med. Chem.* **49**, 6177–6196
77. Sastry, G. M., Adzhigirey, M., Day, T., Annabhimoju, R., and Sherman, W. (2013) Protein and ligand preparation: Parameters, protocols, and influence on virtual screening enrichments. *J. Comput. Aided Mol. Des.* **27**, 221–234
78. Baker, N. A., Sept, D., Joseph, S., Holst, M. J., and McCammon, J. A. (2001) Electrostatics of nanosystems: Application to microtubules and the ribosome. *Proc. Natl. Acad. Sci. U. S. A.* **98**, 10037–10041
79. Dolinsky, T. J., Nielsen, J. E., McCammon, J. A., and Baker, N. A. (2004) PDB2PQR: An automated pipeline for the setup of Poisson-Boltzmann electrostatics calculations. *Nucleic Acids Res.* **32**, W665–W667
80. Watanabe, T., and Honda, K. (1982) Measurement of the extinction coefficient of the methyl viologen cation radical and the efficiency of its formation by semiconductor photocatalysis. *J. Phys. Chem.* **86**, 2617–2619
81. Bernhardt, P. V., Chen, K.-I., and Sharpe, P. C. (2006) Transition metal complexes as mediator-titrants in protein redox potentiometry. *J. Biol. Inorg. Chem.* **11**, 930–936
82. Bernhardt, P. V., Comba, P., Hambley, T. W., and Lawrance, G. A. (1991) Coordination of the sexidentate macrocycle 6,13-dimethyl-1,4,8,11-tetraazacyclotetradecane-6,13-diamine to iron(III). *Inorg. Chem.* **30**, 942–946
83. He, F. M. C., and Bernhardt, P. V. (2017) Cobalt cage complexes as mediators of protein electron transfer. *J. Biol. Inorg. Chem.* **22**, 775–788
84. Neese, F. (2012) The ORCA program system. *WIREs Comput. Mol. Sci.* **2**, 73–78
85. Lenthe, E. v., Wormer, P. E. S., and Avoird, A. V. D. (1997) Density functional calculations of molecular g-tensors in the zero-order regular approximation for relativistic effects. *J. Chem. Phys.* **107**, 2488–2498
86. Lenthe, E. V., Avoird, A. V. D., and Wormer, P. E. S. (1998) Density functional calculations of molecular hyperfine interactions in the zero order regular approximation for relativistic effects. *J. Chem. Phys.* **108**, 4783–4796

Molecular basis of molybdenum enzyme diversification

87. Stoll, S., and Schweiger, A. (2006) EasySpin, a comprehensive software package for spectral simulation and analysis in EPR. *J. Magn. Reson.* **178**, 42–55
88. Dos Santos, J. P., Iobbi-Nivol, C., Couillault, C., Giordano, G., and Mejean, V. (1998) Molecular analysis of the trimethylamine N-oxide (TMAO) reductase respiratory system from a *Shewanella* species. *J. Mol. Biol.* **284**, 421–433
89. Weiss, M. (2001) Global indicators of X-ray data quality. *J. Appl. Crystallogr.* **34**, 130–135
90. Diederichs, K., and Karplus, P. A. (1997) Improved R-factors for diffraction data analysis in macromolecular crystallography. *Nat. Struct. Biol.* **4**, 269–275
91. Assmann, G., Brehm, W., and Diederichs, K. (2016) Identification of rogue datasets in serial crystallography. *J. Appl. Crystallogr.* **49**, 1021–1028